ISPRS Journal of Photogrammetry and Remote Sensing 186 (2022) 34–54

Contents lists available at ScienceDirect

ISPRS Journal of Photogrammetry and Remote Sensing

journal homepage: www.elsevier.com/locate/isprsjprs

Airborne imaging spectroscopy for assessing land-use effect on soil quality in drylands

Nathan Levi [a,b], Arnon Karnieli [a], Tarin Paz-Kagan [b,*]

[a] The Remote Sensing Laboratory, French Associates Institute for Agriculture and Biotechnology of Dryland, Jacob Blaustein Institutes for Desert Research, Sede Boqer Campus, Ben-Gurion University of the Negev, 8499000, Israel
[b] Department of Sensing, Information and Mechanization Systems, Institute of Agricultural Engineering, Agricultural Research Organization (ARO), Volcani Center, Israel

ARTICLE INFO

Keywords:
Soil quality index
Arid environment
Support vector machine-regression
Runoff harvesting system
Agriculture
Grazing

ABSTRACT

Global population growth has resulted in land-use (LU) changes in many natural ecosystems, causing deterioration in the environmental conditions that affect soil quality. The effect of LU on soil quality is acute in water-limited systems that are characterized by insufficient availability of soil organic resources. Thus, the main objective of this study was to assess the effects of human activities (i.e., land-uses as grazing, modern agriculture, and runoff harvesting systems) on soil quality using imaging spectroscopy (IS) in the arid regions of Israel. For this, 12 physical, biological, and chemical soil properties were selected and further integrated into the soil quality index (SQI) as a method to assess the significant effects of LU changes in an arid area in southern Israel. A flight campaign of the AisaFENIX hyperspectral airborne sensor was used to develop an IS prediction model for the SQI on a regional scale. The spectral signatures, extracted from the hyperspectral image itself, were well separable among the four LUs using the partial least squares-discriminant analysis (PLS-DA) classification method (OA = 95.31%, Kc = 0.90). The correlation was performed using multivariate support vector machine-regression (SVM-R) models between the spectral data and the measured soil indicators and the overall SQI. The SVM-R models were significantly correlated for several soil properties, including the overall SQI (R^2_{adj}Val = 0.87), with the successful prediction of the regional SQI mapping (R^2_{adj}Pred = 0.78). Seven individual soil properties, including fractional sand and clay, SOM, pH, EC, SAR, and P, were successfully used for developing prediction maps. Applying IS, and statistically integrative methods for comprehensive soil quality assessments enhances the prediction accuracy for monitoring soil health and evaluating degradation processes in arid environments. This study establishes a precise tool for sustainable and efficient land management and could be an example for future potential IS earth-observing space missions for soil quality assessment studies and applications.

Abbreviations: ANOVA, Analysis Of Variance; ASD, Analytical Spectral Device; AWC, Available Water Content; BRDF, Bidirectional Reflectance Distribution Function; BREFCOR, BRDF Effect Correction; Ca + Mg, Calcium and Magnesium; Cal, Calibration; Cl, Chlorine; EC, Electrical Conductivity; EMR, Electromagnetic Radiation; EPSG, European Petroleum Survey Group; $F_{(df)}$, F-statistic and Degrees of Freedom; FWHM, Full Width at Half Maximum; GPS, Global Positioning System; ICP-MS, Inductively Coupled Plasma-Mass Spectrometer; IMU, Inertial Measurement Unit; IQR, Interquartile Range; IS, Imaging Spectroscopy; K, Potassium; Kc, Kappa Coefficient; LTER, Long-Term Ecological Research; LU, Land-Use; LULC, Land-Use Land-Cover; LV, Latent Variable; MAD, Median Absolute Deviation; MDS, Minimum Data Set; Na, Sodium; NDVI, Normalized Difference Vegetation Index; NIR, Near-Infrared; NIRS, Near-Infrared Reflectance Spectroscopy; $NO3^-$, Nitrate; OA, Overall Accuracy; P, Phosphorus; PC, Principal Component; PCA, Principal Component Analysis; PLS-DA, Partial Least Squares-Discriminant Analysis; PLS-R, Partial Least Squares-Regression; PPS, Predictive Power Score; Pred, Prediction; R^2_{adj}, Adjusted Coefficient of Determination; RBF, Radial Basis Function; RHS, Runoff-Harvesting System; RMSE, Root Mean Square Error; RPD, Ratio of Performance to Deviation; RPIQ, Ratio of Performance to Interquartile Range; SAR, Sodium Adsorption Ratio; SD, Standard Deviation; SMAF, Soil Management Assessment Framework; SNR, Signal to Noise ratio; SOM, Soil Organic Matter; SQI, Soil Quality Index; SSQI, Spectral Soil Quality Index; SVM-R, Support Vector Machine-Regression; SWIR, Shortwave Infrared; Val, Validation; VIP, Variable Importance in Projection; VIS, Visible.

* Corresponding author.
E-mail addresses: nathanle@post.bgu.ac.il (N. Levi), karnieli@bgu.ac.il (A. Karnieli), tarin@volcani.agri.gov.il (T. Paz-Kagan).

https://doi.org/10.1016/j.isprsjprs.2022.01.018
Received 9 September 2021; Received in revised form 7 December 2021; Accepted 21 January 2022
Available online 11 February 2022

1. Introduction

Based on some scenarios, the global population might reach up to 12 billion people by the end of the century (UN-WPP, 2020). Consequently, providing food security and essential ecosystem services is necessary to maintain basic livelihood requirements, including habitat sustainability, shelter, and other necessities (FAO, 2019). Their provision often coerces the transformation of natural ecosystems into human-dominated lands on a global scale (Foley, 2005). Intensive land-use (LU) changes threaten environmental conditions and their ability to support ecosystem services sustainably. Such conditions include regulating natural aspects of climate, water, soil, and air quality (Metzger et al., 2006; Tscharntke et al., 2005). LU changes often engender soil degradation processes and soil quality deterioration (Chesworth, 2008), and soil erosion (Alewell et al., 2019). These degradation processes undermine effective and sustainable land management and its related LU practices (Crist et al., 2017). Soil quality is determined by the ongoing soil physical, biological, and chemical processes occurring above and below the ground, affecting soil conditions (Idowu et al., 2008). In arid regions, the soil system under LU alteration is greatly susceptible to land degradation, such as soil salinization, erosion, structural modification, and organic matter and nutrient imbalance, mainly due to low organic resource and water availability (Lal, 1997).

Thus, appropriate soil quality evaluation approaches are necessary to monitor and mend the overall soil capacity to support ecosystem services (Doran and Parkin, 1994), especially for soils in dryland regions. Soil quality and health assessment protocols, such as the comprehensive assessment of soil health (CASH; Idowu et al., 2008; Moebius-Clune et al., 2016), focus more on agriculture applications. Alternatively, the Soil Management Assessment Framework (SMAF; Andrews et al., 2002; Viscarra Rossel et al., 2006; Wienhold et al., 2009) is a method that allows flexibility in terms of selecting ad-hoc soil indicators under varying environmental conditions. The adoption of SMAF enables the soil quality model to be adjusted to different environments and management applications, as demonstrated in previous studies (Levi et al., 2021; Lima et al., 2016; Paz-kagan et al., 2016). It is based on selecting a minimum data set (MDS), comprising a minimum number of soil indicators (i.e., soil properties) for defining and quantifying soil conditions and function while avoiding model over-complexity. By doing so, the soil quality models are reproducible, easy to sample, and maintained at a relatively low cost (Andrews et al., 2004; Karlen et al., 1997). Once the MDS is selected, the indicators are transformed into a normalized score using different transformation functions, ranging from 0 to 1, then integrated into an index representing the overall soil quality index (SQI) value. In the context of ecological monitoring, resulting overall scores imply the degree of changes in their uninterrupted natural vicinity rather than providing an absolute independent score.

Despite their accuracy, laboratory soil analyses and field surveys are still costly, time-consuming, and labor-intensive (Paz-Kagan et al., 2014). In the past few decades, the development and improvement of the near-infrared reflectance spectroscopy (NIRS) method have proven its efficiency as a rapid, reproducible, and relatively inexpensive method in remote sensing, in general, and soil spectroscopy, in particular, at the point scale. Spectroscopy measures the interactions between the studied surface (e.g., soil sample) and the incident electromagnetic radiation (EMR) by examining highly accurate point spectroscopy reflected signal that includes the visible (VIS, 400–700 nm), near-infrared (NIR, 700–1100 nm), and shortwave infrared (SWIR, 1100–2500 nm) spectral regions (Ben-Dor and Banin, 1995). Soil spectroscopy enables the detection of unique spectral absorption and reflection features (i.e., chromophores) in the spectral signature of a soil sample caused by the vibrations, stretching, and bending responses of soil minerals' elemental and molecular structures to EMR excitation (Ben Dor et al., 2015; Demattê et al., 2007). The use of spectroscopy in soil studies has been on the rise, proving its efficiency and expedience for various soil properties (Bogrekci and Lee, 2005; Freschet et al., 2011; Gholizadeh et al., 2013; Romsonthi et al., 2018; Stafford et al., 2018). In recent years, efforts were made to collect, analyze, and establish worldwide open-access soil spectral libraries that store soil samples, including several fundamental soil properties analyses and their spectral attributes from 92 countries, to facilitate decision-support systems for farmers and land managers on global, continental, and national levels (Chabrillat et al., 2019b; Demattê et al., 2019; Orgiazzi et al., 2018; Shi et al., 2014; Viscarra Rossel et al., 2016). These could be used to train and validate different soil models based on airborne and satellite imaging spectroscopy.

Soil spectroscopy was also most valuable for predicting SQI and other integrative assessment indices (Askari et al., 2015; Cécillon et al., 2009; Cohen et al., 2006; Gozukara et al., 2022; Kinoshita et al., 2012; Levi et al., 2020; Paz-Kagan et al., 2015, 2014; Vågen et al., 2006; Veum et al., 2017, 2015). For example, Kinoshita et al. (2012) estimated a three-category SQI in Western Kenya. Veum et al. (2015) estimated SMAF indicators and scores using VIS-NIR spectra and auxiliary laboratory data. Gozukara et al. (2022) applied an SQI approach using a combination of VIS-NIR-SWIR and pXRF spectrometers to examine the prediction capabilities for SQI and other soil indicators along an entire agricultural soil profile in Turkey. Paz-Kagan et al. (2014) developed the spectral soil quality index (SSQI) to evaluate the overall SQI based solely on spectroscopy. Levi et al. (2020) predicted scores of soil attributes and SQI levels with reasonable accuracy. Currently, the use of hyperspectral data for SQI prediction usually corresponds to a more locale extent since it requires training the model with ground-truthing data according to the local soil characteristics. These applications were mainly demonstrated in temperate climates where the land-use had been changed into a few limited LU practices, mostly agricultural systems. The broad regional implementation is still a challenge due to the high soil spatial/geographical heterogeneity, on the one hand, and a large number of soil samples needed for developing such models. Moreover, studies on soil spectroscopy applications for integrative soil monitoring in hyper-arid, arid, and semi-arid environments are rare (Levi et al., 2020; Paz-Kagan et al., 2014, 2015). In the current research preceding this study, the integration of soil spectroscopy to assess the SQI method was performed in an arid region characterized by a water-scarce, nutrient--poor, and sparsely populated environment, with limited human activity (Levi et al., 2020).

Several statistical approaches incorporate spectroscopy for the regression-based spectral prediction of soil properties. Some algorithms are quite standard, such as partial least squares-regression (PLS-R; Rosero-Vlasova et al., 2016), support vector machine-regression (SVM-R; Shi et al., 2015), geographically weighted regression (GWR; Chen et al., 2019), and multiple linear regression (MLR; Rossel and Behrens, 2010). In recent years, additional models have been used in soil spectroscopy, such as random forest (RF; Wang et al., 2021), artificial neural network (ANN; Ayoubi et al., 2011), and other types of statistical estimation methods. Also, deep-learning neural network-based feature training frameworks have been increasingly used to predict various soil properties spectrally in recent years (Padarian et al., 2019; Singh and Kasana, 2019; Tsakiridis et al., 2020; Yuan et al., 2020). Such deep-learning architectures usually require large sets of previously pre-processed data to reduce the risk of over-fitting (Srivastava et al., 2014). Therefore, conventional machine-learning regression models, such as PLS-R and SVM-R, are adequate for the task of a small-size sampling dataset (Deiss et al., 2020; Thissen et al., 2004). The SVM-R is a well-known method applied in soil spectroscopy that showed previous promising results (de Santana et al., 2021; Thissen et al., 2004; Xuemei and Jianshe, 2013). The statistical approaches affirm the accuracy, time-efficiency, and reliability of spectroscopy for soil quality assessment to determine a spectral sensitivity analysis. These could be applied for individual soil indicators or as integrated indices as SQI. However, the constraints of the soil spectroscopy approach for large-scale monitoring are specified in local point-scale and site-specific studies. Despite its solid quantitative capabilities, these are limited by the relatively small number of sampling points from a particular study

area (Ong et al., 2019).

A limited number of studies have developed soil spectroscopy applications for assessing soil quality in dryland regions. For example, Levi et al. (2020) have successfully applied a spectroscopy-based model of 14 physical, biological, and chemical soil properties, with different accuracy levels, to calculate the statistically integrated SQI based on the SMAF protocol. Yet, one of the limitations of point spectroscopy is that it is related to the point scale and does not account for the spatial variability of the soil. Imaging spectroscopy (IS) compiles a large number of contiguous spectral image bands (>50) as an indirect method to assess soil biochemistry (Ben-Dor et al., 2009). IS method can be applied to soil properties and quality assessments at improved spatial and spectral resolutions, moving from the point-scale to a larger geographical area. The regression models can be used to IS for soil property predictions at a broader scale, based on the integration of soil laboratory analyses and hyperspectral image measurements. In addition, due to many narrow wavebands, IS can be used to highlight unique spectral features, such as the absorption and reflectance of diagnostic wavelengths from the image itself, similar to laboratory spectroscopy analysis (Goetz et al., 1985). For multivariate analysis, sensitivity spectral band selection is derived from the calculated regressions via a variable importance analysis that detects the most effective wavelengths in the correlation process (Cécillon et al., 2008).

Some large-scale mapping methods for different sets of soil properties have been developed. For example, the Land-use/Cover Area frame statistical Survey (LUCAS) topsoil dataset from the European soil data center (ESDAC) provides a mapping of a great variety of soil properties across Europe and over 25 of its countries based on collected and stored soil libraries, partially including spectral measurements (Ballabio et al., 2019). The Australian Commonwealth Scientific and Industrial Research Organization (CSIRO) developed the GlobalSoilMap project, and the data are managed as part of the Australian Soil Resource Information System (ASRIS). This gives access to the "soil and landscape grid" that provides a range of soil and landscape attributes and map products across the country (Johnston et al., 2003). Geo-statistical approaches were also being used to assess soil quality at the regional scale (Rinot et al., 2019). For example, Svoray et al. (2015) suggested a method based on vicarious statistical evaluation and interpolation to quantify soil health in a spatially explicit manner over a large area. Nussbaum et al. (2018) and Hengl et al. (2018) compared several regression and machine-learning methods for statistical prediction assessment of multiple soil properties as part of the digital soil map (DSM) framework (McBartney et al., 2003). However, the incorporation of imaging spectroscopy for soil quality mapping encapsulates significant advantages, such as integrating a large set of soil properties, ground-truthing data, rigorous analytical and statistical evaluation, and the continuous precise mapping over large extents.

Moving from point spectroscopy to image spectral analysis reflects on many challenges that need to be considered. On the practical level, the transition of the SQI model from the local to the regional scale requires a shift from point spectroscopy to an IS approach. Such problems and limitations include a low signal-to-noise ratio (SNR), large and complex datasets, signal interferences from the atmosphere and mixed pixels of the non-soil area due to pixel size (e.g., vegetation and soil crust), the effects of the bidirectional reflectance distribution function (BRDF), and the necessity of highly skilled personnel for processing and analyzing the large datasets. Moreover, airborne IS is still expensive and requires a complex infrastructure to operate (Ben-Dor et al., 2009; Chabrillat et al., 2019a). Despite these drawbacks, the use of airborne IS to study properties and processes related to soil has emerged and grown substantially in the last couple of decades (Chabrillat et al., 2019a), through its mapping and monitoring of multiple aspects such as soil salinity (Ben-Dor et al., 2002; Zhang et al., 2019), soil composition (Li, 2020; Žížala et al., 2017), soil organic carbon (Stevens et al., 2006; Tziolas et al., 2020), soil moisture (Diek et al., 2016; Haubrock et al., 2008), soil erosion and stability (Schmid et al., 2005, 2016), soil contamination (Davies and Calvin, 2017; Pelta et al., 2019), and many other soil aspects.

Paz-Kagan et al. (2014) demonstrated the use of 14 soil indicators in determining the variability of soil attributes among three different LU types that changed from managed to unmanaged and vice versa. They developed the spectral soil quality index (SSQI) based on the point spectroscopy of standard laboratory soil analyses. The SSQI integrates all relevant scored SQI indicators and then classifies them according to their spectral differences. In their following work, Paz-Kagan et al. (2015) have successfully applied and upscaled the SSQI method using the IS approach. They managed to map the overall SQI over several agricultural fields in two different study sites under various LUs and treatments, based solely on the spectral differences between each LU, achieving strong classification values (overall accuracy of 0.92 and 0.82 at the Israeli and German sites, respectively).

The current study attempts to develop the SQI based on IS using machine-learning applications in an arid environment characterized by a water-scarce, nutrient-poor, and sparsely populated environment. The novelty of the research lies in the combination of traditional chemical soil laboratory analyses and the spectral dimension based on imaging spectroscopy (IS) methods to comprehensively evaluate soil quality. It incorporates AisaFENIX airborne IS with advanced statistical analyses to study the ability to determine the soil state on a large scale by measuring the effects on the overall quality of different LUs in dryland regions. Such applicability in extreme conditions like the Avdat region, with various LUs, will exemplify its relevance in temperate climate areas. To accomplish our goals, we considered only the upper layer of the soil due to the ability of the sensor to detect only the soil surface layer. Soil properties change with the soil profile over time under field conditions with responses to soil moisture range. However, the hyperspectral airborne system's limitation could capture only the upper soil surface area. Thus, based on the significant impact LUs have on their natural arid soil surroundings, the main goal of this research is to evaluate their effects over the study area using IS applications. Specifically, the objectives include (1) demonstrating the capability of IS for continuous mapping of multiple soil properties and the integrated SQI over the whole study area; (2) examining the combination of both conventional soil chemical laboratory survey and the contribution of the spectral dimension to the regression-based prediction capabilities of IS; and (3) evaluating the effect of LU change on the soil health patterns in arid regions that include agriculture, grazing, and runoff-harvesting systems (RHSs) for agricultural and forestry purposes on the uninterrupted natural land.

2. Material and methods

2.1. Study area

The current study follows the work conducted by Levi et al. (2020) in the same study area of the Avdat region (Fig. 1). The site is a sparsely populated arid region in Israel's central Negev Desert, and also serves as a long-term ecological research (LTER) station (Fig. 1A; Olsvig-Whittaker et al., 2012). The study area extends over about 24 km^2. The landscape is characterized by barren, steep, and rocky terrain in the western and southern parts, which moderates further northward along the basin of the ephemeral Zin stream, and it consists of sparse vegetation cover (Ohana-levi et al., 2018). As a region characterized by hot, dry summers and cold, low-precipitation winters, soil water retention, available organic material, and soil nutrients are mainly concentrated along the Zin Stream and its basin and are greatly dependent on seasonal rains and runoffs (Ziv et al., 2014). The more developed soil columns are located northwards in the upper parts of the watershed and the lower and flatter parts. These regions consist of generally finer grain-sized colluvium, mostly of loess soil type that can be found as far as several meters deep in the depressed segments, situating it within the aridisol soil order (Yair and Danin, 1980).

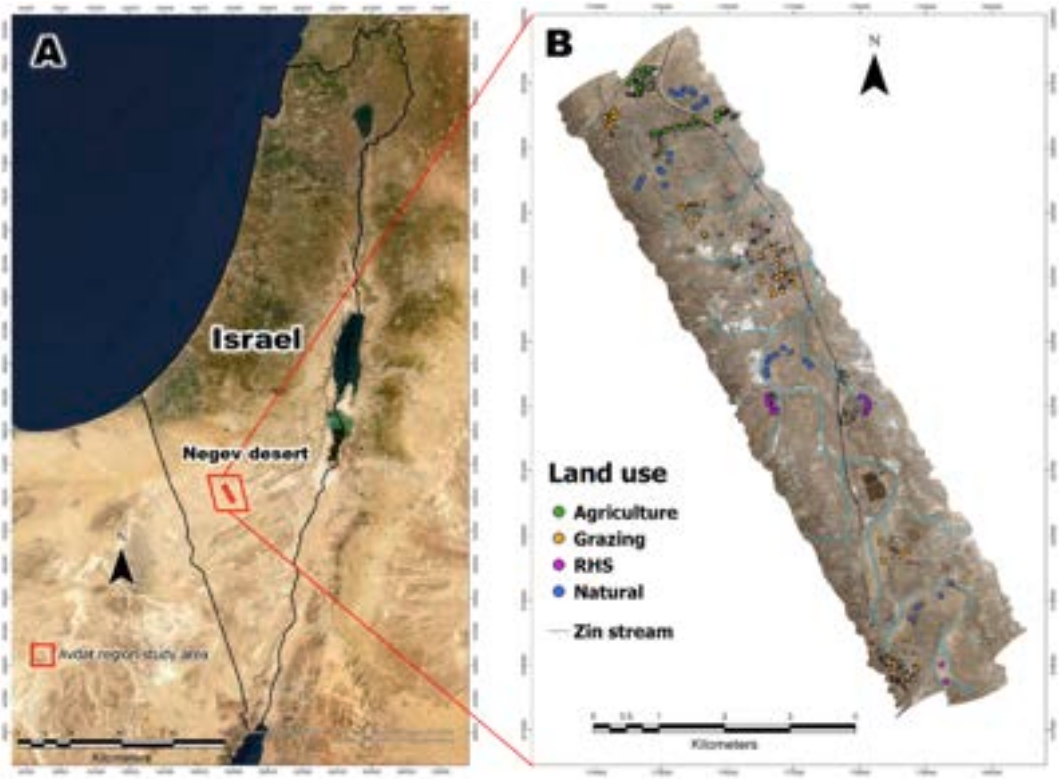

Fig. 1. (A) Location of Avdat region within the Negev Desert, Israel. (B) Soil sampling sites, their respective land-use class, and the Zin Stream channel positioned over the hyperspectral image. Fully detailed information for all sampling sites is presented in Levi et al. (2020). RHS: runoff harvesting system.

The region comprises four LU types, of which three are human-dominated formations: single-family agricultural farms (primarily consisting of grapevine and olive cultivation), RHSs for agricultural and afforestation purposes, and agro-pastoral grazing, mainly of sheep and goats, that takes place in the vicinity of Bedouin villages. The RHSs include two types of human-made landscape structures scattered within or adjacent to the Zin stream. The first is a larger runoff-ponding catchment hedged by soil levees named *limans*, primarily used for afforestation into small-scaled cultivation and as a means of flooding mitigation while improving the soil's productivity by capturing essential environmental resources, notably organic matter, nutrients, sediments, and seeds (Paz-Kagan et al., 2019). The *limans* were mainly developed at the beginning of the 1960's by the Jewish National Fund (JNF) as an afforested grove. The second is streambed stone-wall terraces that retain and regulate runoff flow, infiltration rates, and soil erosion, where some terraces include ancient systems that are still active to this day, while others are abandoned and breached (Yizhaq et al., 2020). The fourth is uninterrupted natural land (Ohana-levi et al., 2018; Paz-Kagan et al., 2017). These ancient terraces cover large dry riverbeds in the Zin Stream's basin, a systematic human intervention in arid landscapes. Terracing was introduced in the Roman (63 BCE–324 CE) and Byzantine (324–640 CE) eras to develop a fertile agro-ecosystem in arid regions. They aimed to improve water retention and soil stabilization and reduce hydrological connectivity and erosion, all of which assists in increasing the primary and secondary productivity of agroecological systems (Beckers et al., 2013).

2.2. Research approach and structure

Fig. 2 presents the general approach of the research framework and assimilates multiple field survey procedures, laboratory analyses, and data processing and interpretation. The research structure includes three steps: (1) in-field soil sampling, chemical soil laboratory analyses, and the SQI development; (2) airborne hyperspectral image acquisition, pre-processing, and spectral data extraction; and (3) IS approach integration of the chemical soil laboratory analysis and spectral data extracted from the IS using SVM-R modeling and large-scale mapping prediction. The following sections describe the methodology performed in each step.

2.3. Step 1: Soil sampling, analysis, and SQI development

2.3.1. Soil sampling and laboratory analysis

The soil collection for further physical, biological, and chemical soil surveys took place in April 2017, initially including 114 soil samples from the upper soil layer (15 cm) of the four LUs taken from 14 sampling sites scattered across the study area covered by the hyperspectral image (Fig. 1B). Sampling locations were defined based on an initial stratified random sampling design (Kothari, 2004), integrating variables such as elevation, lithology, and land-use land-cover (LULC) classification (Ohana-levi et al., 2018). Soil samples were collected from the uppermost 0–15 cm from the ground surface, and each was assigned a location using a handheld GPS device. Further elaboration on the sampling sites and methodology can be found in Levi et al. (2020).

The laboratory soil survey incorporated the analyses of 12 soil properties, following the SMAF protocol (Wienhold et al., 2009), and their respective procedures and methods are specified in Table 1. The selected properties include physical indicators of soil texture (fractional sand, silt, and clay), indicating the morphology and fragmentation of the soil. The available water content (AWC) was calculated by the difference between water holding at field capacity and the soil's permanent wilting point (Scrimgeour, 2008). This is a critical factor for water availability to plants and soil organisms, greatly affected by the changing soil texture types (Groenendyk et al., 2015). The biological indicators included soil organic matter (SOM), which initiates soil processes such as nutrient storage, enzyme activity, carbon stocking, and salinity level moderation (von Lützow et al., 2007). The extractable nitrate (NO_3^-) represents the nitrogen available to the plant in the soil, a fundamental resource for organic life-building blocks (Pansu and Gautheyrou, 2006). The

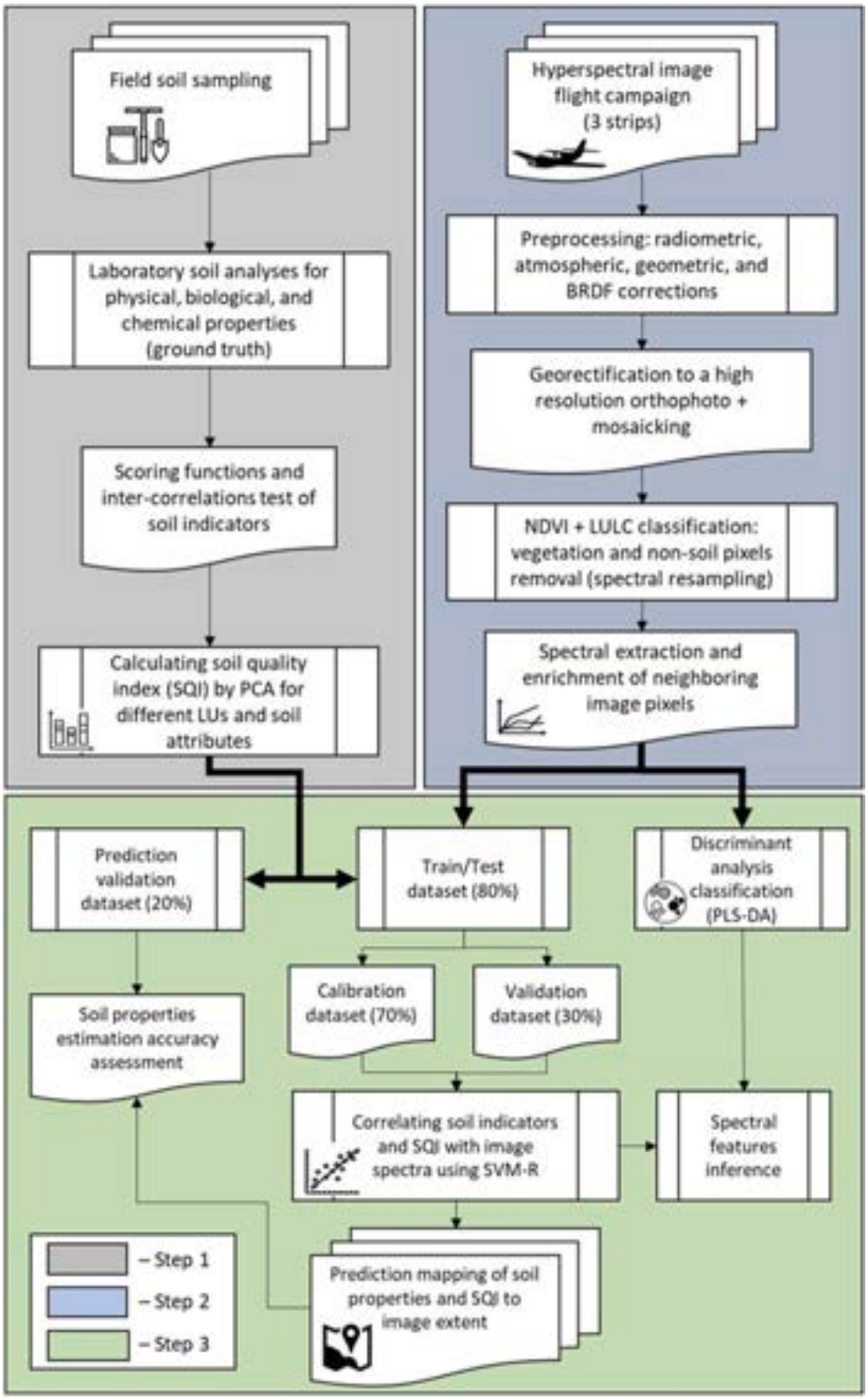

Fig. 2. Study flowchart of the three steps for developing the soil quality assessment model for regional-scale imaging spectroscopy (IS) prediction mapping for individual soil properties and the overall soil quality index (SQI) in Avdat region study area.

chemical indicators include pH, electrical conductivity (EC), extractable chlorine (Cl), extractable sodium (Na), extractable calcium and magnesium (Ca + Mg), and the sodium adsorption ratio (SAR). These properties serve as reliable indicators for soil alkalinity and as precursors of ongoing soil salinization and sodicity processes, on the one hand, and soil micro-aggregation, on the other (Rahimi et al., 2000). The extractable phosphorus (P) and extractable potassium (K) are valuable soil nutrient constituents of proteins and nucleic acids, which are essential components in plant tissue and are crucial in regulating different processes in plants.

2.3.2. *Developing the SQI model*

The development of the SQI includes several statistical and mathematical procedures. One of the main goals of this study is to map SQI and

Table 1
Soil quality properties and their respective affiliation, units of measurement, and analysis methods. A comprehensive review of the applied laboratory survey methods can be found in Levi et al. (2020).

Indicator	Unit	Method
Physical properties		
Soil texture (fractional sand, silt, and clay)	–	Particle size suspension (Kettler et al., 2001)
Available water content (AWC)	%	Oven drying and weight difference (Scrimgeour, 2008)
Biological properties		
Extractable nitrate (NO_3^-)	mg/kg	Potassium chloride extractions (Norman and Stucki, 1981)
Soil organic matter (SOM)	%	Organic carbon furnace method (Casida et al., 1964)
Chemical properties		
Acidity level (pH)	–	1:1 water-soil suspension extraction (Roades, 1982)
Electrical conductivity (EC)	dS/m	
Extractable chloride (Cl)	mg/l	ICP-MS (Brady and Weil, 1999)
Extractable sodium (Na)	mg/l	
Extractable calcium and magnesium (Ca + Mg)	mg/l	
Sodium adsorption ration (SAR)	–	
Extractable phosphorus (P)	mg/kg	
Extractable potassium (K)	mg/kg	

ICP-MS: inductively coupled plasma-mass spectrometer.

soil properties over the whole study area. Therefore, the calculated SQI was developed for the four LUs and their physical, biological, and chemical attributes. First, a minimal amount of outliers were removed, using the median absolute deviation (MAD) method (Leys et al., 2013). The MAD excludes values greater or lower than three standard deviations (SDs) from each of the soil indicators' central median values, resulting in the removal of very few outliers, not exceeding 5% for any soil property. Following that, the soil properties were transformed into unitless scores ranging from 0 (poor performance) to 1 (excellent performance). For each of the selected MDS indicators for the study scheme, one of three non-linear polynomial scoring functions were selected (Eqs. (1)–(3)), for value standardization and comparability (Masto et al., 2007):

$$Si_{more} = \frac{1}{1 + e^{-b(x-a)}} \tag{1}$$

$$Si_{less} = \frac{1}{1 + e^{b(x-a)}} \tag{2}$$

$$Si_{optimum} = 1 \times e^{\frac{-(x-a)^2}{b}} \tag{3}$$

where x is the initial soil indicator value, a is the least square deviation from the mean, and b is the SD's slope of the mean ($2\sigma^2$). "More is better" assigns higher scores to properties with high raw values, notably AWC, SOM, and NO_3^-, for their severe shortage and soil biotic activity propagation. The "Less is better" transformation designates lower concentrations of potentially soil-degrading materials, including EC, Cl, Na, and Ca + Mg, linked to soil salinization processes. The designation of "Optimum" grants higher ranks to observations surrounding the indicator's mean value, incorporating pH, SAR, P, and K, which promote moderate soil acidity and the distribution of soil nutrients (Idowu et al., 2009; Moebius-Clune, 2017). The indicators' adjustment is essential in giving greater significance to prevailing soil processes that strongly affect soil quality than their natural references (Andrews et al., 2004). For this reason, the scoring calculation of soil samples from the agricultural, RHS, and grazing LUs was derived from their nearby natural LU samples by sharing their mean and SD values in the process of the SQI calculation (Masto et al., 2008).

The scored soil indicators were integrated to calculate the ultimate SQI. First, to prevent high collinearity and redundancy in the SQI model, the power predictive score (PPS) was applied for the multiple pairwise correlations amongst all 12 scored soil properties (Wetschoreck et al., 2020). The measured relationships were locally normalized and assigned with a predictive score ranging from 0 to 1. The normalized PPS value expresses the power of their correlation, not only for linear and non-linear patterns in the data but also for the correlation's asymmetry and directionality (i.e., $X \sim Y \neq Y \sim X$). Strongly correlated indicators ($PPS \geq 0.5$) were excluded from further SQI development. Afterward, a principal component analysis (PCA) for statistical calculation of significantly different uncorrelated dimensions (i.e., variables) was performed (Jolliffe et al., 2016). The whole variance of the model was divided into several low-covariable principal components (PCs; Hotelling, 1933), where the number of PCs with eigenvalues (i.e., weighted proportion of variance) is greater than one and accounting for at least 5% of the cumulative variance was examined. The scored soil indicators and their respective allocated statistically distinct weighted PCs were multiplied and summed into the eventual feature-scaled (0–1) SQI score for each soil sample (Eq. (4)):

$$SQI = \sum_{i=1}^{n} PWi \times Si' \tag{4}$$

where PWi is the assigned PC weight, and Si' is the scored soil indicator. The resultant SQIs create a simplified method for comparing and assessing the intensity of the disturbance to the soil samples relative to their natural references. The workflow of the PPS method was imported into R from Python (Zavarella, 2020), using the "reticulate" package (Ushey et al., 2020), and the PCA was performed using JMP® Pro-software version 15.0.0 (SAS Institute Inc., Cary, NC, USA).

2.4. Step 2: Airborne hyperspectral image acquisition and processing

2.4.1. Hyperspectral image acquiring

The following step included applying soil indicators and SQI predictions to a more considerable regional extent. The confirmed results of the previous study were based on point-scale spectroscopy under a controlled laboratory protocol that served as reference ground-truth measurements. In this study, we applied IS as a suitable approach to predict the soil attributes and quality assessment on the regional scale. Accordingly, a flight campaign using an airborne hyperspectral imager obtained a three-striped image, taken under good weather and clear sky conditions over the Avdat study area on April 7, 2017. The AisaFENIX 1 K sensor (Specim, Spectral Imaging Ltd.) was used in the flight campaign to capture the hyperspectral image of the study area. The soil sampling collection was conducted in parallel to the flight campaign. The AisaFENIX scanner holds a single optic aperture mounted onto a light aircraft. The sensor contains 420 contiguous spectral bands across the VIS-NIR-SWIR spectral region, which provides a spectral resolution of 3.5 nm in the VIS-NIR bands (380–970 nm) and 12 nm for the SWIR bands (970–2500 nm) and a full width at half maximum (FWHM) of 3.5–6.5 nm. The sensor was carried at an altitude of 660 m aboveground, which provided an eventual spatial resolution of 1 m per pixel. The ongoing geographical positioning of the aircraft was recorded using an inertial measurement unit (IMU) for further geometric rectification (Brook and Ben-Dor, 2015).

Yet, image-based field measurements are susceptible to signal mixing and interferences caused by various factors, such as angular illumination, surface roughness, atmospheric light scattering, water vapor absorption, topographic orientation, vegetation and stone cover, and sensor radiometric and spectral instability performance (Brook and Ben-Dor, 2015). Hence, the acquired images had to undergo a series of preprocessing and calibration procedures for further analysis to achieve near-laboratory quality reflectance information (Ben-Dor et al., 2009). Using the airborne imagery-induced ATCOR-4 software (ReSe Applications LLC), the radiometric, atmospheric, and topographic corrections

were performed based on the MODTRAN radiative transfer model®. The atmospheric correction was calibrated with ground targets measured by a portable analytical spectral device (ASD), the FieldSpec Pro® spectrometer, as described by Brook and Ben-Dor (2015). Additionally, the BRDF effectcorrection (BREFCOR) was implemented to minimize the BRDF disruptions caused by various surface covers (Schlapfer et al., 2015), resulting in a color-balanced calculated surface reflectance value for the three stripes. In addition, a transformation to the Israeli Grid 05/12 (EPSG:6991) projection was applied, the same correspondent projection for all spatial datasets throughout the research. This was followed by manual georectification to a high-resolution reference orthophoto of the study area (taken in November 2015) for improved positional accuracy. Lastly, the three stripes were unified into one combined image using ENVI software's seamless mosaic workflow, where the geo-rectified hyperspectral image was precisely co-registered with the locations of the soil samples with a total error of <1 m (RMSE = 0.648).

2.4.2. Non-soil pixel exclusion and spectral enrichment

To easily mask out non-soil pixels, the image was first spectrally resampled to Landsat 8 resolution to simplify the image classification in terms of better contrast and spectral separability coherence among the various land-cover features. The spectral resampling was performed by calculating the normalized difference vegetation index (NDVI; Tucker, 1979). The index was calculated using the sensor's NIR and red center wavelengths (864.67 nm and 654.59 nm, respectively; Barsi et al., 2014) for removing pixels of vegetation, built-up areas, and rocks exceeding a $0.05 < NDVI < 0.25$ range value. Although vegetation indices values are universal, the exact limit of certain classes is subjected to vegetation types, local reflectance intensity, vegetation cover, and density, etc. Therefore, this study's threshold was found best to distinguish vegetation pixels from other land-cover types and was decided following a trial and error process. Following this, a land-use land-cover (LULC) classification was performed to define the main land-cover features identified in the area. A supervised minimum distance classification (Wacker and Landgrebe, 1972) was conducted to remove very bright soils related to undeveloped and unconsolidated chalk and marl soils and additional non-soil land-cover categories. The subsequent masked image outline was used to clip the final shape of the original full spectral resolution image.

Furthermore, bands within the spectral range of susceptibility to atmospheric vapor absorption (1350–1490 and 1830–2100 nm) and noisy bands on the spectra fringes (380–439 nm) were excluded from the dataset, resulting in 336 spectral bands in total. Spectral signatures from the adjacent pixels surrounding the initial soil sample locations were extracted (3×3 neighborhoods), enlarging the model's entry to a total of 1,026 points for a development of a pixel-based model. The pixel selection process enabled us to enrich the dataset, reduce spectral heterogeneity, and improve the model's confidence due to varied land surface features and LUs. Each newly added spectral signature was assigned to the corresponding soil laboratory measurement values within its neighboring pixels by incorporating the laboratory and spectral data. The SVM-regression prediction maps were generated for the individual soil indicators and the integrated SQI.

2.5. Step 3: IS approach integration of the laboratory data

2.5.1. Discriminant analysis classification of spectra by land-use

Before integrating the spectral and the chemical laboratory soil survey datasets through a regression process, a classification analysis for the enriched image-extracted hyperspectral data of the four studied land-uses was performed. The spectral differentiation between the land-uses is a primary indication of the applicability of spectroscopy as a suitable assessment tool for further SQI and other individual soil properties regression and prediction. The spectral classification was performed using a partial least squares-discriminant analysis (PLS-DA) method. The PLS-DA is a multivariate linear method that quantifies and categorizes the continuous predictor variable (spectra – X) into different classes of the discrete variable (land-uses – Y). The model creates a hyperspace dimension that splits into statistically distinct components called latent variables (LV). Each LV represents a portion of the total cumulative variance of the observations relating to their respective class membership, which results in a well-defined classification of the multivariate feature hyperspace (Singh et al., 2005). The output of the PLS-DA provides a scatterplot that conveniently graphically illustrates the separability of the observed data according to its predetermined classes, in addition to a statistical evaluation of significant differences between classes. Similar to other classification methods, the performance of the PLS-DA model is also evaluated using overall accuracy (OA) and Kappa coefficient (Kc) metrics. In addition, the PLS-DA also produces comparative variable importance in projection (VIP; Cécillon et al., 2008) analysis to rate the relative significance of each wavelength for the four LUs to detect the most prevalent spectral features in the model. The PLS-DA classification and graphical illustration was performed with MATLAB® PLS_Toolbox (Eigenvector, Wenatchee, Washington, USA; Wise et al., 2006).

2.5.2. Soil chemical properties and SQI regression to hyperspectral image

Once the spectral classification of the model is defined, the model regression can be applied. In this study, the regression models between the collected spectral signatures from the image itself (i.e., pixels) and the measured soil indicators at its location were used to generate the prediction maps using IS. The spectral data extracted from the image consisted of 336 spectral bands with high spectral contiguity that interacted differently with each soil indicator. Some of the soil properties, notably NO_3, EC, SAR, P, and K, had highly skewed distributions of their raw values. Hence, these properties were transformed using a $\log_{10}$ for skewness reduction, achieving an acceptable normalized skewness value ($\gamma < \pm 1$) for the different indicators.

Various regression models have been proven satisfactory for spectral prediction of soil properties, with many attempts to minimize the squared error of the predicted values. In addition, soft-margins SVM-R also tries to reduce the error and conceal the values within a certain threshold around the model's hyperplane (i.e., the model's trend line; Drucker et al., 1997). The controlled amount of slack given to specific regression errors allows better flexibility to optimize the different model parameters for such relatively noisy data (Thissen et al., 2004). The resulting restrained hyperplane and boundary lines can produce an optimal trendline to fit the predicted values with minimized absolute error within the model's margins and constraints (Eqs. (5) and (6)). Optimizing the model's fit included two adjustment hyperparameters that were embedded in its calculation, including epsilon (ϵ), which demarcates the margins' width, and cost (C), which regularizes the accepted tolerance for predicted observations outside of ϵ:

$$MIN\frac{1}{2}||w||^2 + C\sum_{i=1}^{n}\left|\xi_i, \xi_i^*\right| \quad (5)$$

$$|y_i - w_i x_i| \le \epsilon + \left|\xi_i, \xi_i^*\right| \quad (6)$$

where $||w||^2$ is the minimized total squared error, $|\xi_i, \xi_i^*|$ is the original and reprojected absolute deviation from the margin ϵ while subjected to $\xi_i, \xi_i^* \ge 0$, y_i is the target, w_i is the error coefficient, and x_i is the predictor value (Drucker et al., 1997). The SVM-R can be applied in a linear form or in higher-dimensional features that use different kernel functions to transform the non-linear dimension of the input space data into linearly separable feature space predicted observations using the "kernel trick" (Vanschoenwinkel and Manderick, 2005). In the current study, the non-linear Gaussian radial basis function (RBF) kernel method was applied (Eq. (7)), with an additional hyperparameter gamma (γ) that defines the influence rate of the training dataset in terms of distance:

$$K(x, x') = \exp\left(-\gamma \|x - x'\|^2\right) \quad (7)$$

where K is the reprojected kernel location for points x and x', while $\|x\text{-}x'\|^2$ represents the squared Euclidean distance between the two observations (Thissen et al., 2004).

For the model design, the enriched dataset was randomly split into calibration (Cal) and validation (Val) subsets using cross-validation sampling at a 70 to 30 split ratio, respectively (Mourad et al., 2005). However, to better evaluate the robustness of the predicted models and measure their accuracy, an independent validation dataset is needed for subsequent comparison against the final soil properties and SQI prediction maps (Shi et al., 2020). For this purpose, 20% of the 114 raw data points of the individual soil indicators and the calculated SQI (i.e., prior to the dataset spectral enrichment) were set apart, including 23 prediction verification points (Pred). The remaining 80%, including 91 raw observations for each measured soil indicator, was used for cross-validation sampling of Cal/Val models at a 70 to 30 split ratio. The number of initial observations slightly changed for the soil properties that had outliers removed from their raw data, referring to the above-mentioned MAD outlier removal. These were then enriched to 819 points for further prediction by selecting the nine neighboring pixels from the geo-location of the soil samplings. In achieving the optimized SVM-R model parameters, a minimal amount of outliers were excluded from the enriched dataset during the regression process based on the interquartile rule (±1.5*IQR; Iglewicz, 2011). The outlier removal did not exceed a 10% threshold for any of the enriched Cal/Val subsets, where for most indicators, only a few extreme points were excluded.

Each soil attribute was statistically evaluated using the adjusted coefficient of determination for both the calibration and validation datasets (R^2_{adj}Cal and R^2_{adj}Val), as well as for the regression's F-statistic value and degrees of freedom ($F_{(df)}$Cal and $F_{(df)}$Val). The selection of the R^2 assumes that every single variable explains the variation in the dependent variable. The adjusted R^2 tells the percentage of variation explained by only the independent variables that affect the dependent variable, hence, even more, accurate in model performance (Miles, 2005). The root means square errors ($RMSE_{Cal}$ and $RMSE_{Val}$) were calculated as well. The ratio of performance to deviation (RPD), which equates the total variations of the measured indicators with those of the validation data in a standardized scale, was calculated as RPD = SD/$RMSE_{Val}$ for each soil attribute and the SQI (Chang et al., 2001). Despite being widely used as a model performance evaluation metric in soil spectroscopy, the RPD assumes a normal distribution of the examined indicators. In contrast, in many cases, they are prone to a significant degree of skewness. Therefore, a suitable evaluation means was using the IQR of the measured indicators' ratio performance ($RPIQ_{Val}$ = IQR/$RMSE_{Val}$) alongside the RPD values for a more comprehensive review of the model's accuracy (Bellon-Maurel et al., 2010).

The significance of the validation models was ranked as: "excellent" at RPIQ ≥ 3.5, RPD ≥ 2.5, and $R^2 \geq 0.80$; "good" at 3 ≤ RPIQ < 3.5, 2 ≤ RPD < 2.5, and $R^2 \geq 0.70$; "moderate" at 2 ≤ RPIQ < 3, 1.5 ≤ RPD < 2, and $R^2 \geq 0.60$; and "poor" at RPIQ < 2, RPD ≤ 1.5, and $R^2 < 0.60$ (Chang et al., 2001; Veum et al., 2015). However, the RPIQ, RPD, and R^2 values are correlated with one another. Hence, using them as reliable indicators must be accompanied by minimizing the disparity between the error values of both calibration and validation datasets, represented by their respective RMSE, to compare the prediction intervals of the models (Mcbratney and Minasny, 2016). Furthermore, the enrichment of the dataset allocates repeated measurements of the soil indicators to newly extracted spectra from the image. Thus, this might cause potential pseudo-replications in the dataset that artificially increase the total agreement (i.e., R^2 values; Wang et al., 2000) and, subsequently, the performance metrics (i.e., $RPIQ_{Val}$ and RPD_{Val}), to a greater degree than would have resulted from a single-pixel extraction estimation. Therefore, the calibration and validation datasets' error sizes ($RMSE_{Cal}$ and $RMSE_{Val}$) were considered more reliable metrics for the success of the prediction model (Mcbratney and Minasny, 2016), where the appropriate difference was set to 25% between the two. Lastly, a VIP analysis was performed to detect and accentuate spectral features in the SVM-R model. The VIP bands of the SVM-R are compared to those of the PLS-DA to examine their relative correspondence as an additional means of model success evaluation.

2.5.3. Models upscale to the hyperspectral image

The regression models were further used to produce the image-based prediction maps. As the non-linear RBF kernel transformed the SVM-R model into a simple two-dimensional linear system, the upscaling of the retransformed regression models was employed in a linear method over the hyper-layered image (Eq. (8)):

$$y = B + A_1X_1 + A_2X_2 + A_3X_3 + \cdots + A_nX_n \quad (8)$$

where y is the additive predicted soil property (pixel) value, A is the calculated model weighting coefficient for each AisaFENIX waveband X, and B is the model's slope (Lugassi et al., 2017). The output of the transformation assigns each pixel in the image to its respective predicted value, generating regression-based continuous prediction maps of the study area. The adjusted R^2 and RMSE values (R^2_{adj}Pred and $RMSE_{Pred}$, respectively) were calculated to examine the relationship between the excluded independent dataset of the measured soil properties and the SQI and their corresponding pixels' locations on the map within their respective neighborhoods. Indicators with an agreement of R^2_{adj}Pred ≥ 0.7 were considered successfully predicted. The SVM-regression and prediction, including parameter grid-search tuning optimization and upscaling, were performed in RStudio with the "e1071" (Meyer et al., 2019) and "caret" (Kuhn, 2020) packages.

2.6. Statistical analysis

Significant differences between LUs for the calculated overall SQI scores were tested using a one-way analysis of variance (ANOVA) test. For the SQI's physical, biological, and chemical attributes, the non-parametric Kruskal-Wallis test was used, as some of the ANOVA's assumptions for normal distribution of the model's residuals and homoscedasticity of the data were unmet. The significance level for the different LU classes of the overall SQI F-statistic and the subgroups' chi-squared (χ^2) test was determined at $\alpha < 0.05$.

3. Results

3.1. Soil quality index (SQI) development

The descriptive statistics for the individual soil indicators' laboratory analyses and their scoring transformation were performed in the previous study and can be found in Levi et al. (2020). The predictive power score (PPS) correlation matrix for the soil properties (Fig. 3) revealed strong correlations between the various salinity indicators and EC, notably Cl ($PPS_{(Cl \rightarrow EC)} = 0.82$), Na ($PPS_{(Na \rightarrow EC)} = 0.73$), and Ca + Mg ($PPS_{(Ca + Mg \rightarrow EC)} = 0.71$), and between themselves. The EC was left as the only representative salinity indicator to rule out possible collinearity and redundancy in the SQI model. The soil texture properties (i.e., fractional sand, silt, and clay) were based on mineral particle size fragmentation (Schindelbeck et al., 2008). These properties were mostly descriptive parameters and constant in values. Hence, soil texture was excluded (Karlen et al., 2003), leaving the SQI model with 8 out of 12 indicators. A significant correlation was also found between NO_3 and EC ($PPS_{(NO3 \rightarrow EC)} = 0.46$) and the salinity indicators, but eventually, the NO_3 remained in the SQI analysis.

The integrated SQI for all soil samples was generated among the LU practices using the physical, biological, and chemical scored soil properties. The results of the PCA suggest that three PCs, with an eigenvalue greater than one and accounting for more than 10% of the proportion of

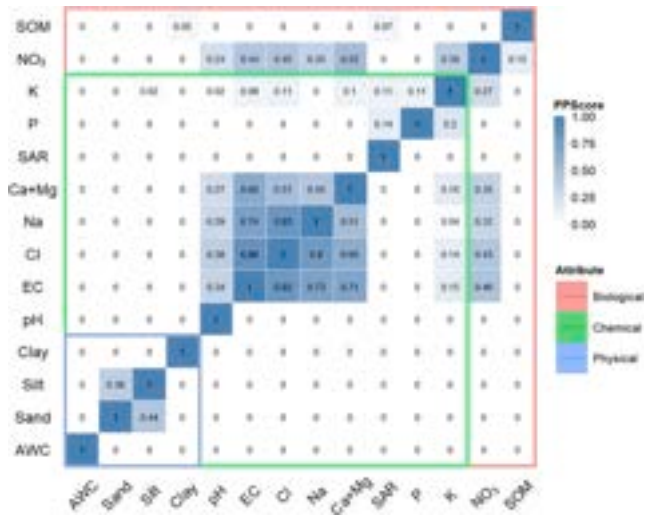

Fig. 3. Predictive power score (PPS) correlation matrix for all the measured soil properties. The colored frames represent the associated physical, biological, and chemical components of the soil indicators. Pairs of soil indicators with high correlations (PPS $\geq$ 0.5) were excluded from further SQI calculation. SQI: soil quality index, AWC: available water content, EC: electrical conductivity, Cl: chlorine, Na: sodium, Ca + Mg: calcium and magnesium, SAR: sodium adsorption ratio, P: phosphorus, K: potassium, NO_3: nitrate, and SOM: soil organic matter.

variance, explained 72.55% of the model's variance (Table 2). PC1 held the most explanatory variance with 40.39% and included the SAR, NO_3^-, P, K, and SOM scored indicators, followed by PC2 with 19.58% of the variation for AWC and EC scores, and PC3 with a loading value of 12.57% for the remaining pH scoring. A PCA bi-plot of the scored soil properties on PC1 versus PC2 is shown in Appendix 1. Fig. 4 displays the mean overall SQI scores and their corresponding physical, biological, and chemical attributes among the four LUs. The mean overall score of all soils combined was SQI = 0.613, whereas the scores for the agriculture, grazing, RHS, and natural LUs were SQI = 0.661, 0.598, 0.566, and 0.605, respectively. Significant differences were found between some of the LUs ($F_{(3)} = 3.59$, $p < 0.05$), where agriculture was significantly higher than grazing ($p = 0.049$) and RHS ($p = 0.02$). Additionally, some significant differences emerged when observing the particular components. The biological soil properties showed the most notable significant differences ($\chi^2_{(3)} = 23.96$, $p < 0.05$), where the natural areas presented significantly lower mean rates (SQI = 0.144) than those of the other three LUs (SQI = 0.230, 0.231, and 0.165 for agriculture, grazing,

Table 2
Principal component analysis (PCA) results for the scored soil indicators. The highest loading factor within each principal component (PC) for every indicator is marked bold.

	PC1	PC2	PC3
Eigenvalue	3.23	1.57	1.01
Proportion of variance (%)	40.39	19.58	12.58
Cumulative proportion (%)	40.39	59.98	72.55
No. of properties	5	2	1
AWC Score	0.16	**0.64**	0.06
NO_3^- Score	**0.85**	−0.39	0.20
SOM Score	**−0.72**	−0.47	0.08
pH Score	−0.19	0.21	**0.86**
EC Score	−0.61	**0.66**	−0.21
SAR Score	**−0.67**	−0.55	−0.06
P Score	**−0.72**	−0.47	0.08
K Score	**0.92**	−0.04	0.08

AWC: available water content, NO_3^-: nitrate, SOM: soil organic matter, EC: electrical conductivity, SAR: sodium adsorption ratio, P: phosphorus, and K: potassium.

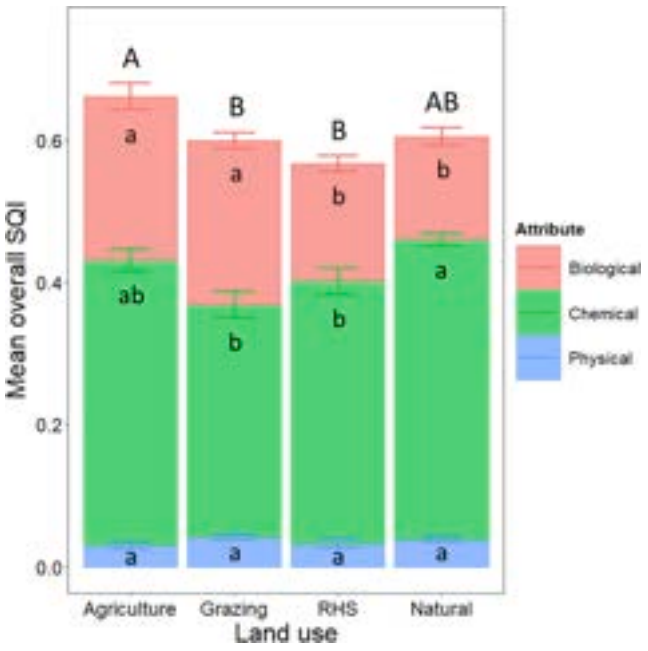

Fig. 4. Mean overall soil quality index (SQI) scores and their respective physical, biological, and chemical indicators' subgroups for the four land-uses (agriculture, grazing, RHS, and natural) in the Avdat study area. Uppercase letters above the error bars indicate significant differences between the land-uses of the overall scores. In contrast, lowercase letters within the bars denote the differences between the particular attributes ($p < 0.05$). RHS: runoff-harvesting system.

and RHS, respectively). On the other hand, the scores' proportion of the chemical attributes ($\chi^2_{(3)} = 12.15$, $p < 0.05$) was significantly higher in the natural LU (SQI = 0.421) than in the grazing and RHS (SQI = 0.327 and 0.368, respectively). The physical subpart showed no significant differences among all four LUs ($\chi^2_{(3)} = 4.58$, $p = 0.21$).

3.2. Hyperspectral image pre-processing

The pre-processing of the hyperspectral image included multiple steps, readying it for further analysis and prediction. Fig. 5 shows the results for the NDVI (Fig. 5A) and the LULC classification map (Fig. 5B) for non-soil pixel exclusion. High NDVI values ($\geq$0.25) indicate vegetation presence, while low and negative values ($\leq$0.05) imply the existence of other non-soil materials, such as rocks, paved roads, and buildings. The land-cover classification for removing additional pixels, including classes of very bright undeveloped chalky soils and built-up areas, resulted in high overall accuracy (OA = 95.11%) and Kappa coefficient (Kc = 0.93) values. The confusion matrix of the minimum distance classification is shown in Appendix 2. The largest 'soil' class that represents the most predominant loess soil in the region accounted for 68.13% of the entire area (16.03 km^2), with 'dark soil' and 'bright soil' classes falling behind (17.11% and 12.63%, respectively). The 'very bright soil' and 'road/built-up' categories cover about 1% of the image each (0.25 km^2). The classification output raised the issue of the BRDF effect's remnants on the image fringes, as the dark soil class suffered from a significantly lower producer's accuracy rate (78.57%; Appendix 2) compared to the rest of the land-cover classes. The western edge of the image was exceedingly attributed to dark soils and very bright soil on the eastern part, while the rest of the image was highly accurate (Fig. 5B), which indicates the effects caused by sun angle directional illumination. Thus, the most extreme interrupted margins of the image were clipped and removed to reduce possible error and prevent further misinterpretation of the results (Fig. 5C). By excluding the NDVI, the LULC classification, and the image fringes, a total of 11.36% of the pixels

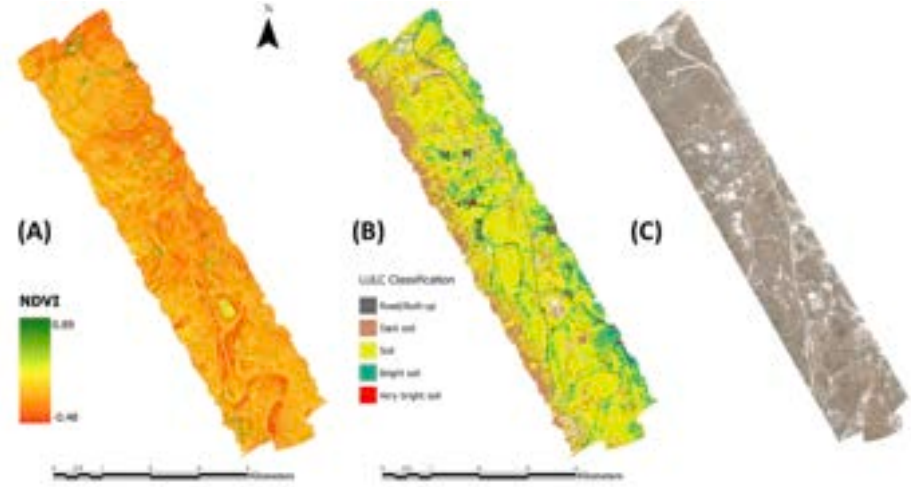

Fig. 5. (A) Normalized difference vegetation index (NDVI); (B) land-use land-cover (LULC) classification map; and (C) final clipped AisaFENIX bare soil image for the Avdat region.

were removed from the image. Once the pre-processing treatments were completed, the corrected and calibrated spectra were extracted from the hyperspectral image. The mean image-extracted spectral signatures of the soil samples for the different LUs are shown in Fig. 6.

3.3. Spectral classification and correlation of SQI and soil indicators

The scatterplot and results of the PLS-DA classification of the image-extracted spectra according to their respective LUs are given in Figs. 6–8. The performed discriminant analysis (Fig. 7) model consists of 3 LVs accounting for 68.25% of the cumulative variance, also exhibiting strong separability among the four LUs (OA = 95.31%, Kc = 0.90). The results indicate a successful classification model that is compatible with further regression and prediction. The variable importance in projection (VIP) analysis was derived from the PLS-DA classification, highlighting unique spectral features (i.e., wavelengths) for each of the examined LUs (Fig. 7). Some significant spectral features were noticed across all LU practices, including 520.69, 792.21, 1537.43, and 2278.13 nm. Others were shared among several LUs, such as 2204.65 nm for agriculture, RHS, and natural, 609.69 and 2441.33 nm for agriculture and grazing, 681.91 and 2405.36 nm for agriculture and RHS, and 2357.12 nm for grazing and natural.

The full results of the SVM-R analysis are presented in Table 3, including the adjusted R^2, RMSE, RPIQ, RPD, F-statistic values, and their significant VIP wavebands for the calibration and validation split datasets. Also, the regression scatterplots for all soil properties are shown in Fig. 9. All the predicted soil indicators and the overall SQI were found significant for image-scale prediction ($RPIQ_{Val} \geq 3$, $RPD_{Val} \geq 2$, and $R^2_{adj}Val \geq 0.70$), except AWC, which presented borderline results ($R^2_{adj}Val = 0.776$, $RPIQ_{Val} = 2.67$, $RPD_{Val} = 2.00$). The overall SQI regression model resulted in an "excellent" degree of validation ($R^2_{adj}Val = 0.867$, $RPIQ_{Val} = 4.09$, $RPD_{Val} = 2.60$, $RMSE_{Cal} = 0.03$, and $RMSE_{Val} = 0.03$). The log-transformed EC ($R^2_{adj}Val = 0.837$, $RPIQ_{Val} = 4.21$, $RPD_{Val} = 2.47$, $RMSE_{Cal} = 0.21$, and $RMSE_{Val} = 0.25$) and P ($R^2_{adj}Val = 0.861$, $RPIQ_{Val} = 4.12$, $RPD_{Val} = 3.19$, $RMSE_{Cal} = 0.10$, and $RMSE_{Val} = 0.12$) exhibited the strongest evaluation metrics of the successfully correlated indicators. The regression models of the fractional sand, NO_3^-, SOM, pH, SAR, and K properties had an "excellent" performance as well. The 25% error ratio (i.e., $RMSE_{Val}/RMSE_{Cal}$) was compromised only by K at 28.12%.

Fig. 10 presents the inclusive variable importance for distinguishing subtle spectral response differences among all soil indicators. A higher VIP score for a particular wavelength implies the existence of a significant spectral feature, where accentuated peaks were noticed across

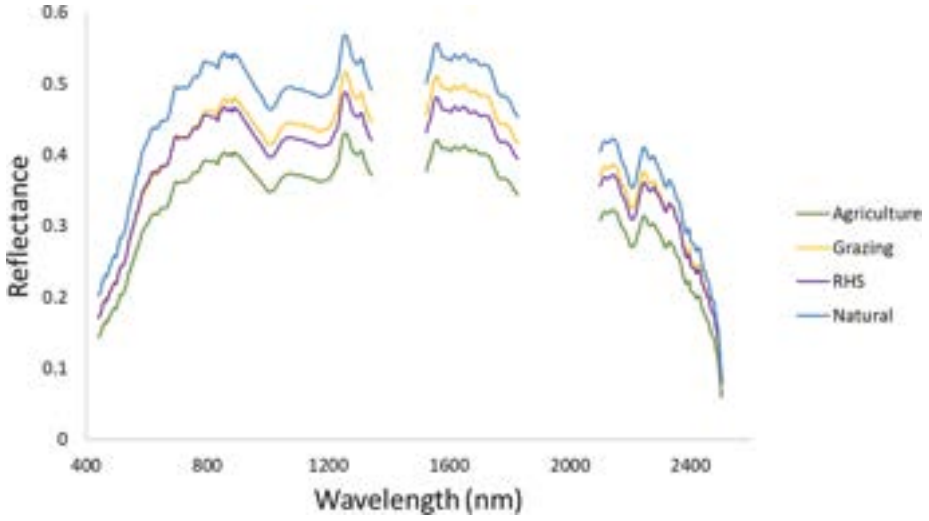

Fig. 6. Mean soil spectral signatures of the four land-use practices (agriculture, grazing, RHS, and natural) extracted from the AisaFENIX hyperspectral image for the Avdat study area. RHS: runoff harvesting system.

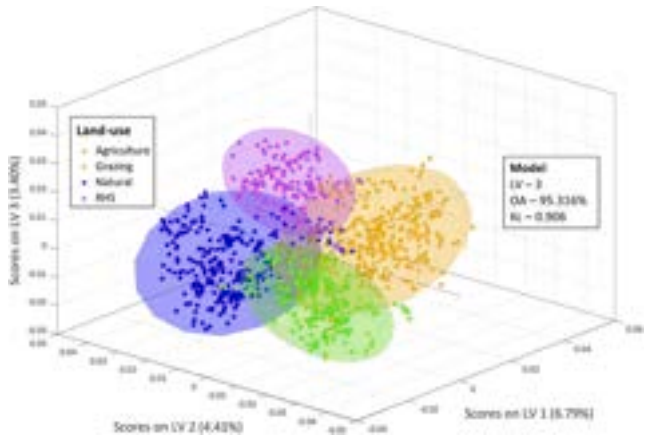

Fig. 7. Partial least squares-discriminant analysis (PLS-DA) classification for the four land-use practices (agriculture, grazing, RHS, and natural) extracted spectra from the AisaFENIX hyperspectral image of the Avdat study area. The figure includes the model's number of latent variables (LV) and the overall accuracy (OA) and Kappa coefficient (Kc) statistics. Colored circles indicate a 95% confidence level. RHS: runoff harvesting system.

different spectral ranges for the soil indicators. Despite the extracted spectra being subjected to noticeable signal disturbances (Fig. 6), recognizable differences between the mean LUs' spectra indicate the soil materials' content variations. The general reflectance is relatively high, referring to the predominant quartz-rich sandy-loam soil texture class, including disparities of specific spectral features. The VIS-NIR range (400–1100 nm) presented some notable VIP attributes: the 680–740 nm range, known for organic matter content, has shared importance for SOM, pH, EC, SAR, and P, and the 870–905 nm is significant for AWC, silt, clay, NO_3^-, and P. However, the SWIR region (1100–2500 nm) showed the most prominent spectral features. The soil moisture absorptions at the 1493.44 nm waveband strongly peaked for AWC, sand, NO_3^-, SOM, EC, P, and K, and at 1593.95 nm for AWC, silt, NO_3^-, pH, and EC, as well as at 2100–2180 nm for AWC, silt, clay, SOM, pH, EC, and K. This was even more so the case for the organic compounds, clay minerals, and carbonates' various absorption attributes across the 2200–2450 nm for almost all soil properties. The spectral regions identified for the SQI model coincide with those of its indicator counterparts, including the 520.69, 678.46, 1593.95, 1763.26, 2223.06, and 2399.35–2435.35 nm wavebands. Most of the regression VIP bands were relatively similar to the spectral regions found by the VIP bands derived from the PLS-DA classification.

3.4. Soil indicators and SQI prediction maps

The final prediction maps for the overall SQI and the individual soil indicators are presented in Figs. 11 and 12, respectively, and their statistical evaluation is given in Table 3 and Fig. 9. For the predicted properties, 8 out of 12 soil indicators were successfully mapped ($R^2_{Pred} \geq 0.7$), including the SQI, fractional sand and clay, SOM, pH, EC, SAR, and P. The map of the overall SQI (Fig. 11A) provided a significant prediction agreement with the excluded verification dataset ($R^2_{adj}Pred = 0.779$, $RMSE_{Pred} = 0.03$), distinguishing well the continuous SQI score patterns in accordance with the different LU practices (Fig. 11B), land-cover features (Fig. 11C), and topography (Fig. 11D).

The successfully upscaled prediction maps of the individual soil indicators (Fig. 12) show that fractional sand and EC had the strongest agreement values ($R^2_{Pred} = 0.853$, $RMSE_{Pred} = 0.05$ and $R^2_{Pred} = 0.84$, $RMSE_{Pred} = 0.32$, respectively), whereas fractional clay and SOM had the most marginal ones ($R^2_{Pred} = 0.706$, $RMSE_{Pred} = 0.02$ and $R^2_{Pred} = 0.722$, $RMSE_{Pred} = 0.43$, respectively). When observing the different properties' maps separately, varying patterns emerge. For example, contradictory trends are observed between the sand and clay maps (Fig. 12A and 10B, respectively), where higher sand concentrations correspond with lower clay fractions. Greater predicted SOM (Fig. 12C) and P (Fig. 12F) contents were observed within and around the interrupted human LU soils and the Zin streambed. A similar trend occurred for pH (Fig. 12D) and EC (Fig. 12E), where both were also affected by the landscape's topographical features. The unsuccessfully predicted properties, including AWC, fractional silt, NO_3^-, and K, all presented poor correlations and large error sizes, and are thus unreliable for soil mapping in this case.

4. Discussion

The current study demonstrated the capability of airborne IS for continuous surface mapping of multiple soil properties and the integrated SQI over the entire study area. The soil properties and overall quality were tested by combining conventional laboratory surveys and the contribution of the spectral dimension to the regression-based prediction capabilities of IS. The incorporation of the laboratory soil analyses of 12 physical, biological, and chemical indicators and the integrated overall SQI with the spectral data extracted from the hyperspectral image was successfully applied. The PLS-DA classification confirmed the strong existing spectral separability among the four examined LUs. The successful classification results enable differentiating between the four LU types and their natural proximity in the arid environment of the Avdat region in the Negev Desert. The prediction of the SQI was found significant for both the local point-scale ($R^2_{adj}Val = 0.87$, $RPIQ_{Val} = 4.09$, $RPD_{Val} = 2.60$, $RMSE_{Cal} = 0.03$, and $RMSE_{Val} = 0.03$) and the large-scale regional mapping ($R^2_{adj}Pred = 0.78$, $RMSE_{Pred}$

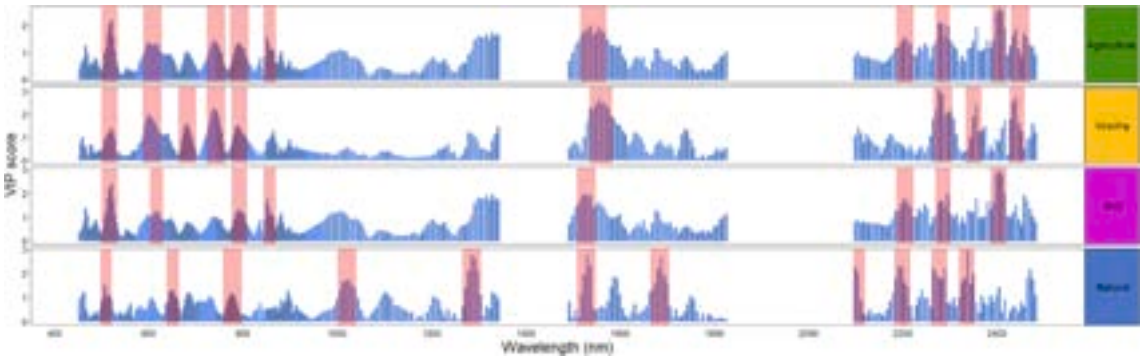

Fig. 8. Variable importance in projection (VIP) plot of the agriculture (green), grazing (orange), runoff-harvesting system (RHS; purple), and natural (blue) land-uses in the Avdat region. Each bar represents the importance score of a particular hyperspectral image waveband in the partial least squares-discriminant analysis (PLS-DA) spectral classification analysis. The red sections highlight regions with spectral features with significant VIP peaks.

Table 3
Support vector machine-regression (SVM-R) analysis and image upscaling of prediction results of Avdat region. For each of the soil properties in the model, the number of support vectors (SVs), the adjusted coefficient of determination for the calibration and validation datasets (R^2_{adj}Cal and R^2_{adj}Val), as well as for the F-statistic value and degrees of freedom ($F_{(df)}$Cal and $F_{(df)}$Val), and the root mean square error ($RMSE_{Cal}$ and $RMSE_{Val}$) were assigned. The ratio of performance to deviation (RPD_{Val}) and the interquartile range ($RPIQ_{Val}$) for the validation set was also calculated. Properties with significant prediction values ($RPIQ_{Val} \geq 3$, $RPD_{Val} \geq 2$, and $R^2_{adj}Val \geq 0.7$) were examined for variable importance in projection (VIP) wavebands, upscaled to the image extent, and were assigned R^2 and RMSE (R^2_{Pred} and $RMSE_{Pred}$). Model constraints and optimization parameters' cost (C), epsilon (ϵ), and gamma (γ) are noted.

Soil properties	R^2_{adj}Cal	R^2_{adj}Val	$RPIQ_{Val}$	RPD_{Val}	SVs	C	ϵ	γ	$F_{(df)}$Cal	$F_{(df)}$Val	$RMSE_{Cal}$	$RMSE_{Val}$	VIP bands (nm)	R^2_{adj}Pred	$RMSE_{Pred}$
AWC (%)	0.844	0.776	2.671	2.005	245	275	3.2	6	$_{(1,552)}$3108	$_{(1,222)}$844.1	3.005	3.673	881.78, 1493.44, 1593.95, 1731.94, 2099.81 2351.07	0.417	4.127
Fractional Sand	**0.913**	**0.817**	**3.681**	**2.528**	**198**	**200**	**0.045**	**1.3**	**5946$_{(1, 568)}$**	**1017$_{(1,235)}$**	**0.035**	**0.044**	**999.77, 1493.44, 1537.43, 1769.52, 2265.92, 2351.07, 2405.36**	**0.854**	**0.047**
Fractional Silt	0.901	0.810	3.491	2.218	214	300	0.04	1	5094$_{(1, 563)}$	1018$_{(1,237)}$	0.032	0.045	881.78, 1537.43, 1593.95, 2180.05, 2417.37, 2471.15	0.494	0.061
Fractional Clay	**0.903**	**0.785**	**3.245**	**2.313**	**205**	**200**	**0.019**	**0.4**	**5210$_{(1, 561)}$**	**861$_{(1,234)}$**	**0.017**	**0.022**	**871.45, 1285.57, 2124.54, 2223.06, 2357.12, 2417.37**	**0.707**	**0.024**
NO_3^- (log_{10})	0.924	0.875	4.545	2.685	248	340	0.16	1.1	6638$_{(1, 547)}$	1548$_{(1,220)}$	0.157	0.206	898.97, 1493.44, 1593.95, 1706.87, 1763.26, 2375.25, 2417.37	0.520	0.422
SOM (%)	**0.925**	**0.848**	**3.718**	**2.625**	**220**	**150**	**0.42**	**3**	**6747$_{(1, 544)}$**	**1218$_{(1,217)}$**	**0.355**	**0.458**	**681.91, 1493.44, 2124.54, 2357.12, 2447.30**	**0.723**	**0.434**
pH	**0.923**	**0.851**	**4.043**	**2.569**	**258**	**125**	**0.12**	**3.2**	**6745$_{(1, 563)}$**	**1277$_{(1,223)}$**	**0.101**	**0.136**	**493.43, 599.39, 681.91, 1018.96, 1593.95, 2112.18, 2417.37**	**0.733**	**0.136**
EC (log_{10})	**0.899**	**0.837**	**4.213**	**2.473**	**220**	**250**	**0.25**	**2.2**	**4909$_{(1, 550)}$**	**1174$_{(1,227)}$**	**0.208**	**0.254**	**688.88, 1025.35, 1493.44, 1537.43, 1593.95, 2167.73**	**0.843**	**0.319**
SAR (log_{10})	**0.902**	**0.842**	**3.573**	**2.637**	**219**	**175**	**0.15**	**1.1**	**5166$_{(1, 560)}$**	**1208$_{(1,225)}$**	**0.136**	**0.158**	**737.04, 1706.87, 2204.65, 2278.13, 2453.27**	**0.783**	**0.170**
P (log_{10})	**0.944**	**0.862**	**4.119**	**3.191**	**245**	**275**	**0.11**	**1.5**	**9221$_{(1, 542)}$**	**1378$_{(1,220)}$**	**0.098**	**0.119**	**602.83, 737.04, 905.85, 1203.38, 1493.44, 2345.02, 2417.37**	**0.733**	**0.101**
K (log_{10})	0.948	0.841	4.490	2.555	226	350	0.21	3.3	10220$_{(1, 562)}$	1179$_{(1,221)}$	0.166	0.231	837.02, 1493.44, 2112.18, 2235.32, 2411.37	0.338	0.450
Overall SQI	**0.901**	**0.867**	**4.085**	**2.602**	**186**	**250**	**0.034**	**0.6**	**5118$_{(1, 560)}$**	**1484$_{(1,226)}$**	**0.028**	**0.032**	**520.69, 678.46, 1317.13, 1593.95, 1688.07, 1763.26, 2223.06, 2399.35–2435.35**	**0.779**	**0.036**

AWC: available water content, NO_3^-: nitrate, SOM: soil organic matter, EC: electrical conductivity, SAR: sodium adsorption ratio, P: phosphorus, K: potassium, and SQI: soil quality index.

= 0.03). We found high prediction ability for seven soil indicators, including fractional sand and silt, SOM, pH, EC, SAR, and P. The developed regional extent mapping enabled the recognition and monitoring of the contiguous spatial variability of different soil processes in response to both human-made practices and environmental features as one. The results provided by the IS methodology affirm its substantial advantages, effectiveness, and reproducibility capabilities for comprehensive soil quality assessment, particularly in rough and challenging arid environments, as in our case study.

4.1. Soil quality assessment

The assessment of soil quality within an ecological scope requires the selection and adjustment of a particular set of soil indicators that will best depict the function of the soil under changing LUs and management practices (Bünemann et al., 2018). The SMAF protocol (Andrews et al., 2004) was most suitable for this objective by employing chemometrics analyses of 12 physical, biological, and chemical soil indicators. As described in the previous study (Levi et al., 2020), soil indicators were selected according to the investigated arid study area and LUs. Therefore, selecting adequate soil indicators and their amount is a great challenge, especially in a resource-limited dryland environment. For instance, plant and microbiome available water, soil organic matter, nutrients, and seed banks in the soil are critically limiting factors in this climate type (Saygin, 2018). Thus, the quantification of their presence is crucial for the soil quality evaluation due to their essential role as precursors of the soil's ability to support the ecosystem's productivity and function (Lal, 2011). It is also necessary to trace soil salinization processes by measuring salinity indicators, such as EC, SAR, and other particular saline elements (i.e., Cl, Na, and Ca + Mg). The loess-dominated aridisol soil order cannot be defined as highly alkaline in its natural state, but rather as a natric subgroup of typical soils (Singer, 2007). However, the salinity levels have shown significant fluctuations in the different LUs practiced, particularly those involved with intensive cropping and herding. Soil texture is also an important property since, in most cases, it strongly dictates other mechanisms within the soil column. Some notable processes include water and organic matter holding capacity, drainage, permeability, fertility (Weil and Brady, 2017), and the support of developing aggregates that improve the soil's resistance and stability, which mitigate its erosion and quality degradation (Eldridge et al., 2020; Levi et al., 2021).

The potential redundancy amid the selected soil indicators in the SQI model was reduced with the exclusion of the strongly correlated salinity properties (i.e., Cl, Na, and Ca + Mg) and the descriptive soil texture, the scoring transformations, and the PCA for a better interpretation of the interrelationships between the selected indicators. The preventive measures taken have confirmed that the incorporated soil indicators were, in fact, statistically distinct and explain most of the variation in the assessment model. The PCA results were used to assign the weights to the transformed scored indicators to develop the statistically integrated SQI for a numerical and quantifiable evaluation of the soil performance in response to the different LUs and land-cover features. The significant differences found for the calculated SQI (Fig. 4) suggest that the human LU practices significantly impact the natural surroundings for the overall estimation in both improvement and degradation. The strictly regulated agricultural fields had higher SQI scores than the grazing and RHS LUs, which are more affected by sporadic processes of livestock behavior and climatic conditions, respectively, with the natural LU placed in-between. Moreover, the significant differences observed between the LUs, mainly for the biological and chemical attributes, revealed a more explicit site-specific depiction of the ongoing soil processes. The biological soil properties were significantly less abundant in the RHS and natural land than in the managed agricultural and grazing practices.

In contrast, the chemical indicators more strongly influenced the natural soils than the other three LUs. This is a direct outcome of the

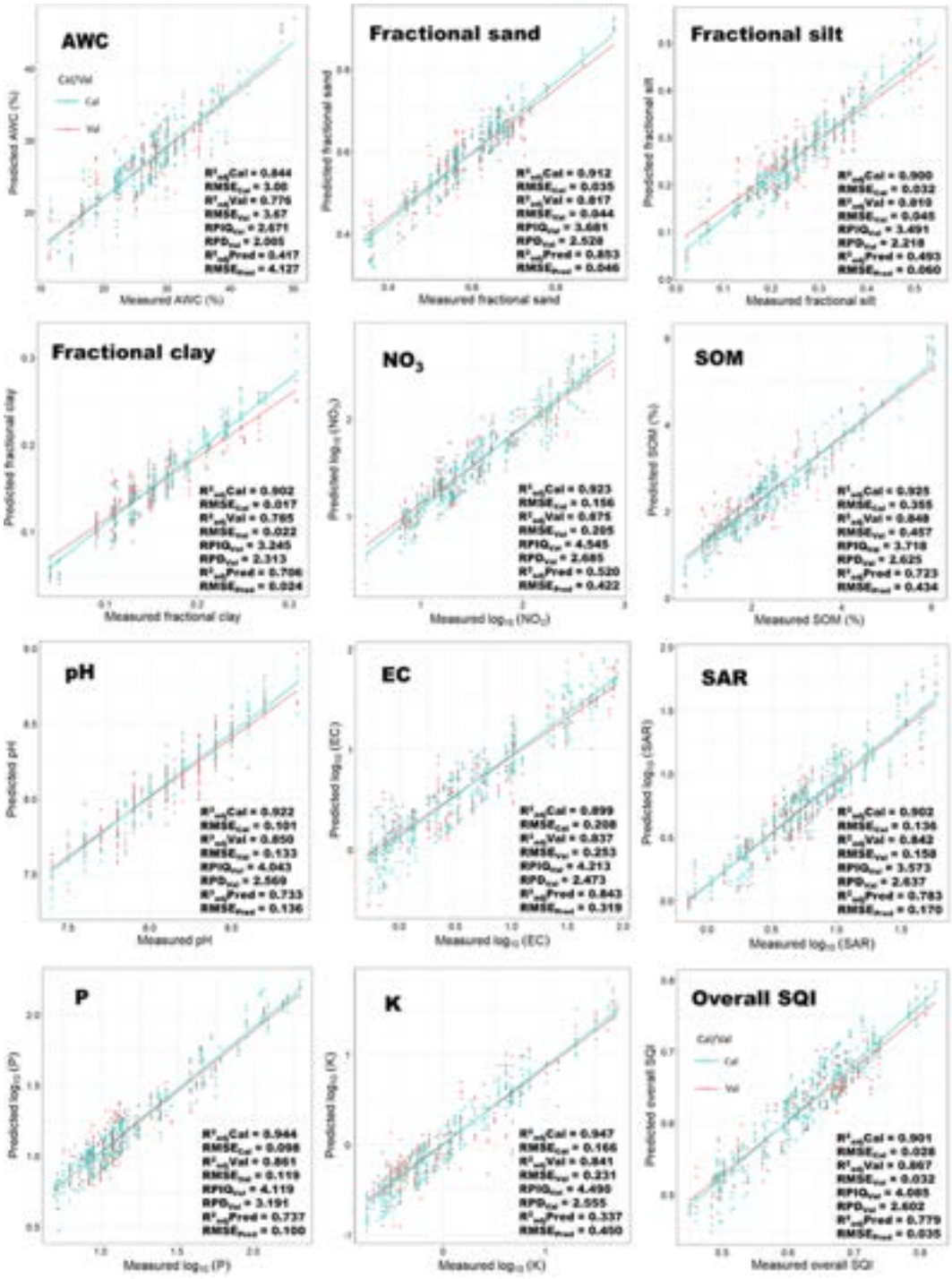

Fig. 9. Support vector machine-regression (SVM-R) scatterplots and main results for the correlated soil properties and the overall soil quality index (SQI), between the measured calibration (Cal) and the validation (Val) datasets, and also the results of the upscaled image prediction maps (Pred). RMSE: root mean square error; RPIQ: ratio of performance to interquartile range; RPD: ratio of performance to deviation; AWC: available water content, NO_3^-: nitrate, SOM: soil organic matter, EC: electrical conductivity, SAR: sodium adsorption ratio, P: phosphorus, and K: potassium.

different agricultural, grazing, and RHS-related inputs, such as irrigation, catchment water, fertilizers, pesticides, organic matter, and livestock residues (Biagetti et al., 2021; Haynes and Naidu, 1998; Turner, 1998). These practices show that the agriculture LU is generally more affected by chemical properties related to cropping activity. At the same time, the grazing LU is more impacted by biological factors derived from livestock and herding activities. On the other hand, the RHS relies on the accumulation of transported natural resources from a severely resource-scarce environment, thus exhibiting significantly low biological properties values, similar to the natural environment.

4.2. *Spectral discriminant analysis classification by LU*

The described PLS-DA classification presents good visual and statistical spectral separability among the four different LU practices. The PLS-DA provides a quantitative approach to separate the cumulative probability of the soil spectral samples into statistically distinct classes, according to their respective LU. The strong classification results

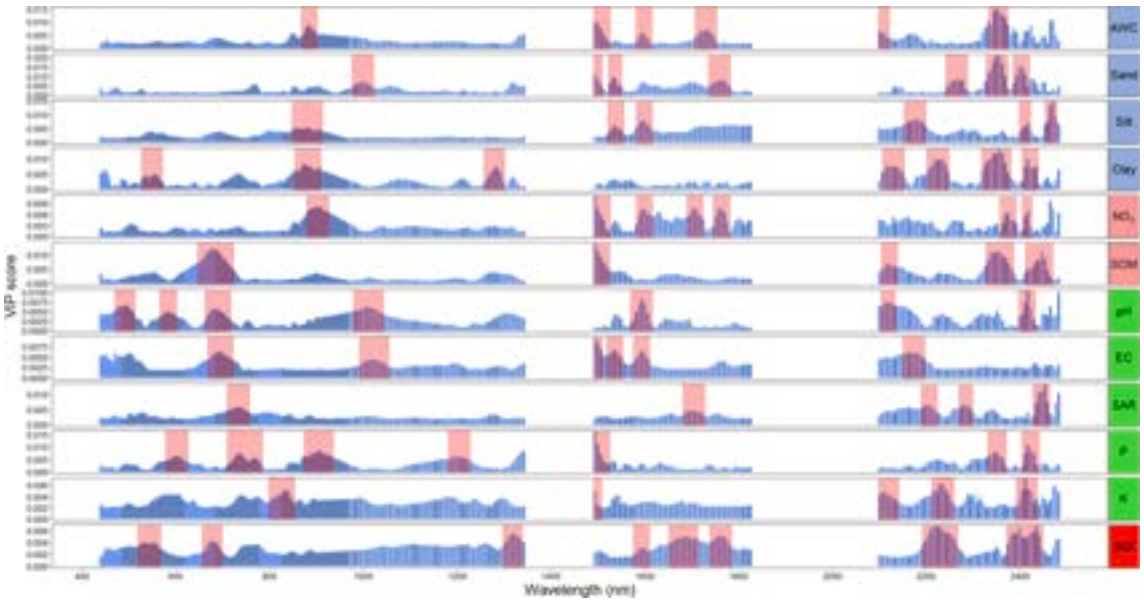

Fig. 10. Variable importance in projection (VIP) plot of the physical (blue), biological (pink), and chemical (green) soil properties in the Avdat region. Each bar represents the importance score of a particular hyperspectral image waveband in the support vector machine regression (SVM-R) analysis. The red sections highlight spectral regions with significant VIP peaks. AWC: available water content, EC: electrical conductivity, Cl: chlorine, Na: sodium, Ca + Mg: calcium and magnesium, SAR: sodium adsorption ratio, $NO3^{-}$: nitrate, P: phosphorus, and SQI: soil quality index. (For interpretation of the references to color in this figure legend, the reader is referred to the web version of this article.)

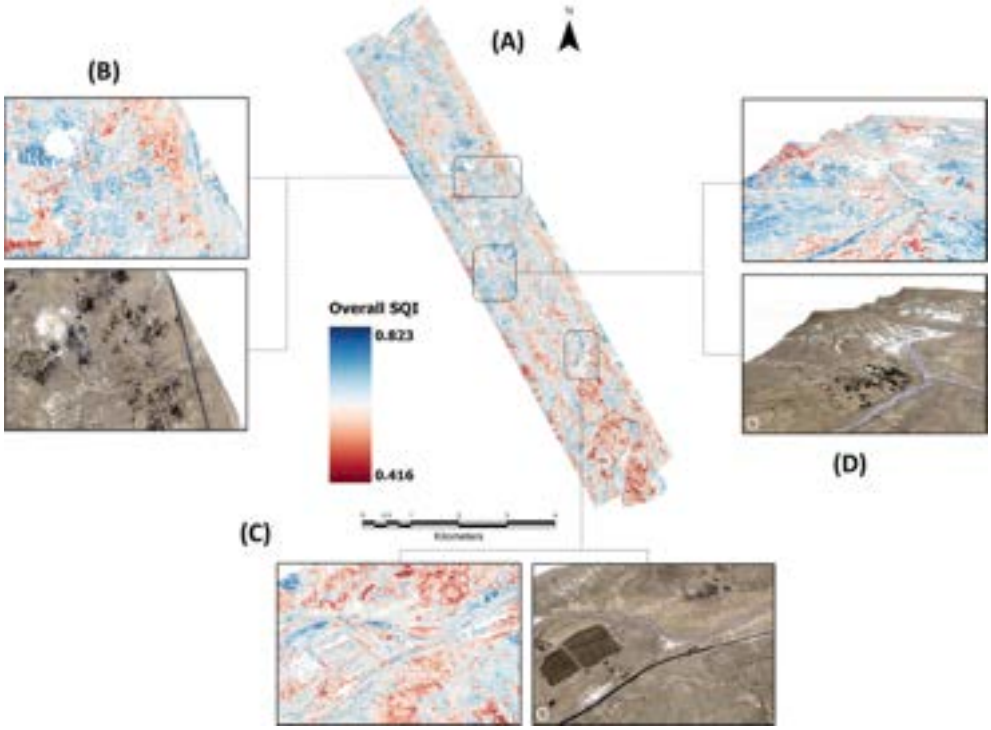

Fig. 11. (A) Final upscaled prediction map for the overall soil quality index (SQI) over the Avdat region, affected by various LU features, including (B) grazing LU and highly eroded bright chalky soil around an unrecognized Bedouin village; (C) agricultural fields (on the left edge of the image), stone-wall terraces (on the right), and the Zin Stream (in the center); and (D) a liman runoff-harvesting system (RHS) and degraded soil in response to steep and barren topography.

presented clear contrast between the different practices, with minor confounding among parts, like grazing mixing with RHS and natural LUs. This could be explained by the fact that these practices share properties that are related to the soil condition and its management. The VIP analysis contributes an additional aspect of the differences among the four practices. While all LUs show sensitivity for shared regions across the spectral range, the particular practices accentuate specific absorption features that imply more significant soil properties. The agriculture displays more significant peaks in the SWIR region (2200–2450 nm), related to organic compounds, clay minerals, and carbonates, in comparison to spectral attributes in the VIS-NIR region (520–850 nm) that are more significantly affected by soil organic

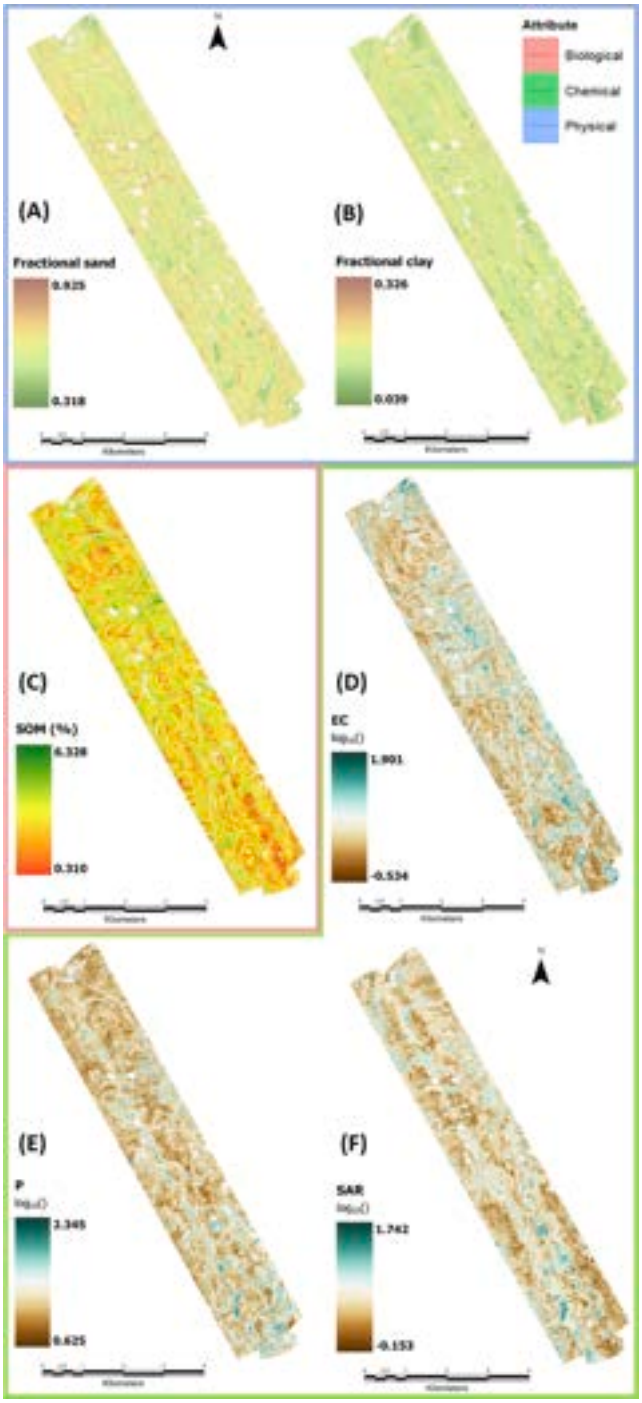

Fig. 12. Final upscaled prediction maps for the individual soil properties over the Avdat region: (A) fractional sand, (B) fractional silt, (C) soil organic matter (SOM), (D) electrical conductivity (EC), (E) phosphorous (P), and (F) sodium adsorption ratio (SAR). The colored frames represent the associated physical, biological, and chemical components of the soil indicators.

matter, nutrients, and herding activity prevailing in intensive grazing soils (Ben Dor et al., 2015). The RHS and natural LUs show a more mixed behavior, where the natural land is less affected by SOM and organic resources due to their scarcity compared to the RHS, but also exhibits more emphasized peaks related to clay minerals (1688.07 nm) and water absorption (1285.57 and 1537.43 nm) for the natural areas (Ben-Dor, 2011).

4.3. Spectral correlations to soil indicators and the SQI

The SVM-R correlations of the measured laboratory soil indicators (i.e., raw and log-transformed) with the enriched extracted spectra from the AisaFENIX image have achieved successful validation values for the SQI ($RPIQ_{Val} \geq 3$, $RPD_{Val} \geq 2$, and $R^2_{adj}Val \geq 0.70$) and several soil properties (Fig. 9 and Table 3). Some showed more robust performances than others, notably EC, pH, NO_3^-, P, and K, representing variations of salinity levels and nutrient availability in the soil. The deviations in the mentioned indicators were firmly attributed to human interference originating from agriculture, grazing, and RHS activities and their effects on the SQI (Paz-kagan et al., 2016; Paz-Kagan et al., 2017). The influence of SOM and AWC is strongly related to soil texture (sand, silt, and clay fractions). Larger fractions of the finer grain-sized clay particles and minerals generally improve their retention capacity within the soil system (Marques et al., 2019). As can be seen from the mean extracted spectra by LU in Fig. 6, the interrupted LU curves are less reflective than the natural ones, indicating the more significant influence and absorption of different artificial effects on the soil. Managed land cultivation increases the inputs and accumulation of vital resources such as water, nutrients, sediments, and seeds. Their increasing abundance in the soil strengthens the absorption factor in the particular spectral regions linked to these soil materials and attenuates the general spectral signature curves of the human LUs compared to the natural ones (Demattê et al., 2007; Stoner and Baumgardner, 1981).

The spectral inference indicates on strengthens of these relationships, where significant spectral features in the SQI regression VIP analysis were affiliated to particular chromophores (Fig. 10). The spectral features in the VIP were associated, regarding various molecular bonds, overtones, and mineralogical structures, with the different soil attributes (Ben-Dor, 2011). For example, EC shows substantially important spectral features in the 1490–1590 and 2200 nm spectral regions, partially, with almost all soil indicators, including AWC, silt, clay, and SOM. These soil properties (i.e., AWC, silt, clay, and SOM) are well-known for their direct or indirect relations to hygroscopic water absorption (Ben Dor et al., 2015), hydroxyl functional O–H group minerals (Taylor, 2004), and carbonate C–O group minerals (Ben-Dor and Banin, 1995). These were mainly related to calcite and dolomite that loosely cement the sedimentary loess soil in this arid region (Shapiro, 2006). The topsoil's retention was also attributed to the soil texture and mineralogical structure and composition. Significant portions of phyllosilicate 2:1 clay and fine silt minerals (e.g., kaolinite and montmorillonite) generate greater pore area for improved water holding capacity and greater soil colloid surface for adsorption of organic matter, soil nutrients, and saline elements (Barré et al., 2008; Barton and Karathanasis, 2005). In turn, these elemental and molecular interactions regulate the exchange capacity of the mineral's electric charge that could potentially undermine the soil's aggregation stability, which eventually results in soil weathering and quality degradation (Conforti et al., 2013).

Different soil properties were acknowledged for various spectral absorption features across the entire spectral range, most notably in the SWIR region (Demattê et al., 2007). Organic matter is known for its direct absorption across the VIS-NIR region around 550–1100 nm and peaking at 675 nm, according to He et al. (2009). The SOM revealed a strong peak at 681.91 nm, along with other indicators, including EC, pH, SAR, and P. These soil indicators were related to colloid adsorption competitors that are accentuated by indirect features in the SWIR over 2300–2450 nm, where SOM moderates the salinity levels when retained in place of saline elements (Ding et al., 2020). Significant features were found within 520–600 nm that associates higher concentration of P with crop and plant residues as well as with some oxides in the soil (Morón and Cozzolino, 2007). The important peaks for K at 2112.18 and 2235.32 nm, which are more prevalent in human LUs than in natural ones, are linked to clay minerals and SOM that supply exchangeable cations (Demattê et al., 2017). The SQI regression model complies with

other individual indicators' success, where significant spectral footprints affect the SQI importance analysis. These emphasized the most predominant features that imply the intercorrelation of the different soil properties (Paz-Kagan et al., 2015). They also correspond well with the acknowledged spectral features found for the PLS-DA classifications VIP analysis. However, it also seems that some unrelated VIP peaks were observed for some of the properties that could not be attributed to the known spectral absorption features of specific materials. The spectral enrichment is a possible reason for introducing particular non-elemental spectral features into the variable importance analysis. These features might originate from site-specific factors such as local topography, which might be responsible for some of the prediction models' inaccuracies.

4.4. Soil quality mapping

The final step towards a comprehensive soil quality assessment is the regional prediction based on the acquired and processed airborne AisaFENIX hyperspectral image. Integrating the extensive soil quality assessment of the physical, biological, and chemical indicators with IS allows inferring the causes of spatial variations for the SQI and soil indicators (Paz-Kagan et al., 2015). The SQI map agreed with the independent soil samples and their corresponding extracted predicted values. It managed to distinguish various clusters of pixel values in the matter of different LUs and terrain features, such as livestock pens and intensive grazing (Fig. 11B), agricultural fields, stone-wall terrace effects, stream paths (Fig. 11C), hillslopes, a *liman*, and underdeveloped soils (Fig. 11D). The spatial divergence was found significant for the SQI and seven other soil properties.

The general trend is that lower and flatter surfaces, like those around the ephemeral Zin Stream, with more developed soil systems, present higher SQI values than the more rugged and steep topography at the study area's western and southern borders. The stream channel itself displayed relatively high SQI scores, with significantly higher rates in locations of deposited fine sediments, such as point and channel bars and stream banks along the meandering stream path (Hu et al., 2017). Along with the discharged deposits, the intensive flashflood events that characterize the region carry soil, organic matter, and mineral nutrients that enrich the soil, improving soil quality (Yang et al., 2019). The RHSs located alongside the stream path showed different trends according to the type of water catchment system observed. The primary function of an RHS is to capture the water and sediment flow that would otherwise wash out of the watershed during runoff-generating rainfall events. The *liman* systems collect the runoff, sediments, and essential soil materials into small catchment areas. Studies have shown that *limans* generally exhibit better SQI score characteristics (Paz-Kagan et al., 2019, 2017). They act as sinks that prevent discharge back to the stream and significantly improve soil quality in small catchment areas (Paz-Kagan et al., 2017). The hydrological barriers of the stone-wall terraces reduce water conductivity and water leakage while increasing soil deposits and moisture on the watershed scale. A general decrease in SQI is detected as the stream attenuates northwards since the terraces effectively reduce the energy of the runoff flow. The upstream terraces dilute a significant amount of the transported soil, resulting in decreased SQI in the downstream watershed (Biagetti et al., 2021; Yizhaq et al., 2020). Studies of terraced riverbeds revealed their essential function in agricultural systems and the conservation of abandoned riverbeds to prevent soil erosion and fertility loss. Our research demonstrates that integrating human-designed water harvesting systems into nature is possible when knowledge on watershed ecology is available. This knowledge can produce a sustainable human-ecological management policy by enhancing services without modifying their inherent properties.

Within the other human-impacted LUs and their surroundings, different variabilities in SQI scores occurred. The modern agriculture fields exhibit diverse patterns among and within plots, which vary in response to applied treatments, irrigation, fertilization, and crops (Ohana-levi et al., 2018). Like the agricultural areas, our results show that the livestock settlements impacted SQI centroids that gradually decreased with distance. These hotspots of degraded SQI scores within the grazing LU are centered mainly around livestock pens, animal waste fills, poor land cultivation, and excessive organic matter accumulation in the feeding areas (Amiri et al., 2008). In contrast, less affected in-between soils exhibited relatively good SQI values.

The overall SQI map depicts the variation in soil processes derived from its assembled individual soil indicators. The EC map accorded well with the SQI map. Higher salinity was observed in weathered and disintegrated soils (i.e., very bright chalk and marlstone) and soils in proximity to Bedouin villages, and steep exposed hillslopes correlated with poor SQI scores. Soil brightness could be an explanatory factor for the bright chalky soils, where a positive correlation was found between soil whiteness and high salinity levels (da Rocha Neto et al., 2017; Moreira et al., 2015). The highly SQI-ranked *limans* profited from the low predicted salinity levels. However, some agricultural LU and stone-wall terrace presented high predicted EC values and high SQI scores. It could be assumed that other indicators took precedence over EC in influencing the overall soil quality within these closed systems. In this regard, the SAR and P (and the poorly predicted K) maps show a similar trend of high predicted values in the agro-systems mentioned above that correlate with lower SQIs. This matching trend can refer to the PCA results (Table 2 and Appendix 1), where both SAR and P were found to be the most significant properties under PC1 and showed very similar factor loadings, with EC placed only under PC2. High measured SAR values imply an excessive sodium content in irrigation water and other fertilizers that act as potential adsorptions to the soil particles, which risks causing soil sodicity. High sodicity levels in the soil can deteriorate the water infiltration rate and hydraulic conductivity, limiting the plant available water and eventually presenting hazards to the soil health (Robbins, 1984).

The SOM distribution was mainly concentrated in some of the agricultural fields and the nearby agro-pastoral settlements. Much of the soil organic compound concentration is derived from cropping and herding occurring along the Zin Stream, as seen by the precipitation of transported organic material across the streambed in the SOM predicted map. The large-scale prediction value of SOM reached an agreement of 0.723, close to the 0.71 predicted SOM mapping value presented by Ou et al. (2021) over a study area in China. For its decisive role in the hydrological properties and material retention in the soil, the soil texture was found significant for both sand and clay. The predominant sandy-loam texture of the region found a high prediction accuracy for sand abundance (R^2_{adj}Pred = 0.853), compared to more temperate climates with loam and silt-loam soil textural classes in Germany (0.77; Kanning et al., 2016) and the Czech Republic (0.67; Žížala et al., 2017), but with a significantly lower agreement for smaller clay fractions (0.706) compared to clay-rich soils in Brazil (0.78; Bellinaso et al., 2021).

Although most detected elements were linked to spectral features recognized by previous literature, we found that other signal interferences caused some additional peaks. These could originate from mixed pixels, surface brightness, the BRDF effect, restricted image spatial resolution, and the remnants of residual organic and non-soil material common in relatively noisy data of this kind (Ben-Dor et al., 2009; Schlapfer et al., 2015). Achieving a color-balanced multi-striped hyperspectral image is highly challenging and assumes an inherited degree of BRDF error for such rugged terrain with multiplex viewing and illumination angles (Jia et al., 2020). A specific gradient was observed for the BRDF disruption, despite removing the image fringes. Increased interference and striping appeared in models with weaker prediction accuracy, meaning significant prediction models were robust enough to overcome the BRDF impediment to present a credible contiguous soil property representation.

Nevertheless, the quantitative capabilities of IS for large-scale soil monitoring, in general, and soil quality assessment, in particular, have proved to possess strong prediction competence. IS applications were

recognized as being a comprehensive, time-efficient, non-destructive, and reproducible analytical approach. At this point, the sensors are mostly airplane-carried and restricted to a specific regional spatial extent due to the current lack of operational hyperspectral satellite platforms (Ong et al., 2019). However, this is starting to change as various soil-induced high signal-to-noise ratio spaceborne imaging spectrometer missions embark on their first steps in orbit to make their acquired imagery accessible for future studies (Chabrillat et al., 2019a). Such missions include: the Italian–Israeli SHALOM (Spaceborne Hyperspectral Applicative Land and Ocean Mission) with 10-m spatial resolution and 240 spectral bands scheduled for 2024 (Feingersh and Dor, 2015); the Italian PRISMA (PRecursore IperSpettrale della Missione Applicativa) launched in March 2019 with 30 m per pixel and 238 bands (Loizzo et al., 2018); the French HypXIM provisioned for 2021 with pixel width starting from 8 m and 210 bands (Michel et al., 2011); the German EnMAP (Environmental Mapping and Analysis Program) planned for 2021 containing 30-m resolution and 228 wavebands (Guanter et al., 2015); the International Space Station (ISS) mounted NASA's HyspIRI (Hyperspectral InfraRed Imager) with 30 m pixel size and 210 bands in 2018 (Lee et al., 2015); and the Japanese HISUI (Hyperspectral Imager SUIte) in December 2019 with 30-m resolution and 185 spectral bands (Matsunaga et al., 2013). The current research could stimulate potential soil studies and questions in future hyperspectral earth-observing space platforms for soil applications at regional and global scales.

5. Conclusion

The effects of LU changes, derived from ancient and modern human activity and disturbance of the natural environment, are crucial in ecological preservation and environmental health monitoring, in general, and for soil quality assessment. The impact of these land transformations is particularly acute when they occur in harsh resource-limited arid conditions such as the Avdat region in Israel's Negev Desert. In this study, a novel approach was developed for soil quality assessment by applying the IS method for a large-scale continuous and precise mapping of the overall SQI and individual soil indicators over the entire study area, particularly under extreme arid climate conditions. The assessment was based on the regression of the measured indicators and the highly detailed spectral information collected from an acquired hyperspectral image. The image-extracted spectra were first classified to examine their inherent separability among the four tested land-uses. Then the soil properties and the overall SQI were correlated using SVM-R, which managed to predict the measured SQI well on the local point-scale and the predicted regional mapping. As a result, seven soil properties were successfully mapped over the entirety of the Aisa-FENIX image. The significantly predicted regional maps have depicted the most prevalent soil-forming and degrading processes causing various environmental disturbances, both natural and human-made, affecting the land and the soil quality through different mechanisms. Many challenges are associated when using IS, like adjusting the assessment model to changing types of soils, climates, scales, and land-uses, as well as overcoming limitations derived from the imaging process, such as high operational costs and the lack of continuous image acquisition over time for long-term monitoring. Despite all these, the strong quantitative capabilities of IS affirm its accuracy, time-efficiency, scalability, and reproducibility even in challenging dryland conditions. This study underscores the applicability of IS for soil function examination under a large variety of environmental conditions and scales, which could be an essential tool for sustainable and efficient land management in degraded land.

Declaration of Competing Interest

The authors declare that they have no known competing financial interests or personal relationships that could have appeared to influence the work reported in this paper.

Acknowledgments

This project has received funding from the European Union's Horizon 2020 research and innovation program "European Long-Term Ecosystem, Critical Zone, and Socio-Ecological systems Research Infrastructure PLUS" (eLTER PLUS) under grant agreement no. 871128. The authors wish to thank Mr. Alexander Goldberg for soil collection, analysis, and logistical support in the field and laboratory work, Dr. Natalia Panov and Dr. Jisung Chang for hyperspectral images preprocessing, and Mr. Vladislav Dubinin for statistical and methodological advice.

Appendices.

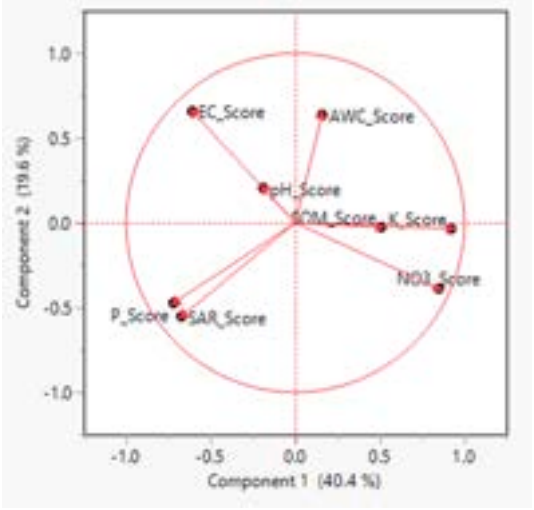

Appendix 1: Principal component analysis (PCA) bi-plot demonstrating the loading factor of the different scored soil indicators for the interactions

of PC1 and PC2. AWC: available water content, $NO3^{-}$: nitrate, SOM: soil organic matter, EC: electrical conductivity, SAR: sodium adsorption ratio, P: phosphorus and, K: potassium.

Appendix 2: Confusion matrix of the land-use land-cover (LULC) minimum distance classification for the AisaFENIX hyperspectral image, resampled to Landsat 8 spectral resolution (Fig. 5B).

Class	Observed					Producer accuracy (%)	User accuracy (%)	Overall agreement rate
Predicted	Very bright soil	Bright soil	Soil	Dark soil	Road/Built-up			
Very bright soil	**1599**	150	0	0	8	99.69	91.01	**Total accuracy:** 95.11%**Kappa (Kc):**0.928
Bright soil	5	**4126**	77	3	72	95.13	96.33	
Soil	0	40	**12450**	680	0	99.36	94.53	
Dark soil	0	16	3	**3156**	9	78.57	99.12	
Road/Built-up	0	0	0	147	**2959**	97.05	95.27	
Total	1604	4337	12530	4017	3049	100	100	
Area (km^2)	0.25	4.03	16.03	2.97	0.25	23.53		
% of total area	1.08	12.63	68.13	17.11	1.05	100		

Appendix A. Supplementary material

Supplementary data to this article can be found online at https://doi.org/10.1016/j.isprsjprs.2022.01.018.

References

Alewell, C., Borrelli, P., Meusburger, K., Panagos, P., 2019. Using the USLE: Chances, challenges and limitations of soil erosion modelling. Int. Soil .Water Conserv. Res. 7 (3), 203–225. https://doi.org/10.1016/j.iswcr.2019.05.004.

Amiri, F., Ariapour, A., Fadai, S., 2008. Effects of livestock grazing on vegetation composition and soil moisture properties in grazed and non-grazed range site. Journal of Biological Sciences 8, 1289–1297. https://doi.org/10.3923/jbs.2008.1289.1297.

Andrews, S.S., Karlen, D.L., Cambardella, C.a., 2004. The Soil Management Assessment Framework: A Quantitative Soil Quality Evaluation Method. Soil Sci. Soc. Am. J. 68, 1945–1962. https://doi.org/10.2136/sssaj2009.0029.

Andrews, S.S., Mitchell, J.P., Mancinelli, R., Karlen, D.L., Hartz, T.K., Horwath, W.R., Pettygrove, G.S., Scow, K.M., Munk, D.S., 2002. On-farm assessment of soil quality in California's Central Valley. Agron. J. 94 (1), 12–23.

Askari, M.S., O'Rourke, S.M., Holden, N.M., 2015. Evaluation of soil quality for agricultural production using visible–near-infrared spectroscopy. Geoderma 243–244, 80–91. https://doi.org/10.1016/J.GEODERMA.2014.12.012.

Ayoubi, S., Pilehvar, A., Mokhtari, P., Sahrawat, K.L. 2011. Application of Artificial Neural Network (ANN) to Predict Soil Organic Matter Using Remote Sensing Data in Two Ecosystems, in: Biomass and Remote Sensing of Biomass. InTech. http://doi.org/10.5772/18956.

Ballabio, C., Lugato, E., Fernández-Ugalde, O., Orgiazzi, A., Jones, A., Borrelli, P., Montanarella, L., Panagos, P., 2019. Mapping LUCAS topsoil chemical properties at European scale using Gaussian process regression. Geoderma 355, 113912. https://doi.org/10.1016/j.geoderma.2019.113912.

Barré, P., Velde, B., Fontaine, C., Catel, N., Abbadie, L., 2008. Which 2:1 clay minerals are involved in the soil potassium reservoir? Insights from potassium addition or removal experiments on three temperate grassland soil clay assemblages. Geoderma 146 (1-2), 216–223.

Barsi, J., Lee, K., Kvaran, G., Markham, B., Pedelty, J., 2014. The Spectral Response of the Landsat-8 Operational Land Imager. Remote Sens. 6, 10232–10251. https://doi.org/10.3390/rs61010232.

Barton, C., Karathanasis, A., 2005. Clay Minerals. Encycl. Soil Sci. Second Ed. https://doi.org/10.1201/noe0849338304.ch57.

Beckers, B., Berking, J., Schütt, B., 2013. Ancient Water Harvesting Methods in the Drylands of the Mediterranean and Western Asia. eTopoi. J. Anc. Stud. 145–164.

Bellinaso, H., Silvero, N.E.Q., Ruiz, L.F.C., Accorsi Amorim, M.T., Rosin, N.A., Mendes, W.de S., Sousa, G.P.B. de, Sepulveda, L.M.A., Queiroz, L.G. de, Nanni, M.R., Demattê, J.A.M., 2021. Clay content prediction using spectra data collected from the ground to space platforms in a smallholder tropical area. Geoderma 399, 115116. https://doi.org/10.1016/j.geoderma.2021.115116.

Bellon-Maurel, V., Fernandez-Ahumada, E., Palagos, B., Roger, J.-M., McBratney, A., 2010. Critical review of chemometric indicators commonly used for assessing the quality of the prediction of soil attributes by NIR spectroscopy. TrAC, Trends Anal. Chem. 29 (9), 1073–1081. https://doi.org/10.1016/j.trac.2010.05.006.

Ben-Dor, E., 2011. Characterization of Soil Properties Using Reflectance Spectroscopy, in: Hyperspectral Remote Sensing of Vegetation. CRC Press, pp. 513–558. http://doi.org/10.1201/b11222-31.

Ben-Dor, E., Banin, A., 1995. Near-Infrared Analysis as a Rapid Method to Simultaneously Evaluate Several Soil Properties. Soil Sci. Soc. Am. J. 59 (2), 364–372. https://doi.org/10.2136/sssaj1995.03615995005900020014x.

Ben-Dor, E., Chabrillat, S., Demattê, J.A.M., Taylor, G.R., Hill, J., Whiting, M.L., Sommer, S., 2009. Using Imaging Spectroscopy to study soil properties. Remote Sens. Environ. 113, S38–S55. https://doi.org/10.1016/j.rse.2008.09.019.

Ben-Dor, E., Patkin, K., Banin, A., Karnieli, A., 2002. Mapping of several soil properties using DAIS-7915 hyperspectral scanner data-a case study over clayey soils in Israel. Int. J. Remote Sens. 23 (6), 1043–1062. https://doi.org/10.1080/01431160010006962.

Ben Dor, E., Ong, C., Lau, I.C., 2015. Reflectance measurements of soils in the laboratory: Standards and protocols. Geoderma 245–246, 112–124. https://doi.org/10.1016/j.geoderma.2015.01.002.

Biagetti, S., Alcaina-Mateos, J., Ruiz-Giralt, A., Lancelotti, C., Groenewald, P., Ibañez-Insa, J., Gur-Arie, S., Morton, F., Merlo, S., 2021. Identifying anthropogenic features at Seoke (Botswana) using pXRF: Expanding the record of southern African Stone Walled Sites. PLoS One 16, e0250776. http://doi.org/10.1371/JOURNAL.PONE.0250776.

Bogrekci, I., Lee, W.S., 2005. Spectral phosphorus mapping using diffuse reflectance of soils and grass. Biosyst. Eng. 91 (3), 305–312.

Brady, N.C., Weil, R.R., 1999. Soil organic matter. In: The Nature and Properties of Soils.

Brook, A., Ben-Dor, E., 2015. Supervised Vicarious Calibration (SVC) of Multi-Source Hyperspectral Remote-Sensing Data. Remote Sens. 7, 6196–6223. https://doi.org/10.3390/rs70506196.

Bünemann, E.K., Bongiorno, G., Bai, Z., Creamer, R.E., De Deyn, G., de Goede, R., Fleskens, L., Geissen, V., Kuyper, T.W., Mäder, P., Pulleman, M., Sukkel, W., van Groenigen, J.W., Brussaard, L., 2018. Soil quality – A critical review. Soil Biol. Biochem. 120, 105–125. https://doi.org/10.1016/j.soilbio.2018.01.030.

Casida, L.E., Klein, D.A., Santoro, T., 1964. Soil Dehydrogenase Activity. Soil Sci. 98 (6), 371–376. https://doi.org/10.1097/00010694-196412000-00004.

Cécillon, L., Cassagne, N., Czarnes, S., Gros, R., Brun, J.-J., 2008. Variable selection in near infrared spectra for the biological characterization of soil and earthworm casts. Soil Biol. Biochem. 40 (7), 1975–1979. https://doi.org/10.1016/j.soilbio.2008.03.016.

Cécillon, L., Es, B., Gomez, C., Ertlen, D., Génot, V., Hedde, M., Stevens, A., Brun, J.-J., 2009. Assessment and monitoring of soil quality using near infrared reflectance spectroscopy (NIRS). Eur. J. Soil Sci. 60, 770–784. https://doi.org/10.1111/j.1365-2389.2009.01178.x>.

Chabrillat, S., Ben-Dor, E., Cierniewski, J., Gomez, C., Schmid, T., Van Wesemael, B., 2019. Imaging Spectroscopy for Soil Mapping and Monitoring 40, 361–399. http://doi.org/10.1007/s10712-019-09524-0.

Chabrillat, S., Gholizadeh, A., Neumann, C., Berger, D., Milewski, R., Ogen, Y., Ben-Dor, E., 2019b. Preparing a soil spectral library using the Internal Soil Standard (ISS) method: Influence of extreme different humidity laboratory conditions. Geoderma 355, 113855. https://doi.org/10.1016/j.geoderma.2019.07.013.

Chang, C., Laird, D., Mausbach, M.J., 2001. Near-Infrared Reflectance Spectroscopy – Principal Components Regression Analyses of Soil Properties Near-Infrared Reflectance Spectroscopy – Principal Components. http://doi.org/10.2136/sssaj2001.652480x.Rights.

Chen, L., Ren, C., Li, L., Wang, Y., Zhang, B., Wang, Z., Li, L., 2019. A Comparative Assessment of Geostatistical, Machine Learning, and Hybrid Approaches for Mapping Topsoil Organic Carbon Content. ISPRS Int. J. Geo-Inf 8, 174. https://doi.org/10.3390/ijgi8040174.

Chesworth, W., 2008. Encyclopedia of soil science/edited by Ward Chesworth., Encyclopedia of soil science, Encyclopedia of earth sciences. Springer, Dordrecht.

Cohen, M.J., Dabral, S., Graham, W.D., Prenger, J.P., Debusk, W.F., 2006. Evaluating ecological condition using soil biogeochemical parameters and near infrared reflectance spectra. Environ. Monit. Assess. 116 (1-3), 427–457. https://doi.org/10.1007/s10661-006-7664-8.

Conforti, M., Buttafuoco, G., Leone, A.P., Aucelli, P.P.C., Robustelli, G., Scarciglia, F., 2013. Studying the relationship between water-induced soil erosion and soil organic matter using Vis-NIR spectroscopy and geomorphological analysis: A case study in southern Italy. Catena 110, 44–58. https://doi.org/10.1016/j.catena.2013.06.013.

Crist, E., Mora, C., Engelman, R., 2017. The interaction of human population, food production, and biodiversity protection. Science 356 (6335), 260–264.

da Rocha Neto, O., Teixeira, A., Leão, R., Moreira, L., Galvão, L., 2017. Hyperspectral remote sensing for detecting soil salinization using ProSpecTIR-VS aerial imagery and sensor simulation. Remote Sens. 9 (1), 42. https://doi.org/10.3390/rs9010042.

Davies, G.E., Calvin, W.M., 2017. Mapping acidic mine waste with seasonal airborne hyperspectral imagery at varying spatial scales. Environ. Earth Sci. 76, 1–14. https://doi.org/10.1007/s12665-017-6763-x.

de Santana, F.B., Otani, S.K., de Souza, A.M., Poppi, R.J., 2021. Comparison of PLS and SVM models for soil organic matter and particle size using vis-NIR spectral libraries. Geoderma Reg. 27, e00436. https://doi.org/10.1016/j.geodrs.2021.e00436.

Deiss, L., Margenot, A.J., Culman, S.W., Demyan, M.S., 2020. Tuning support vector machines regression models improves prediction accuracy of soil properties in MIR spectroscopy. Geoderma 365, 114227. https://doi.org/10.1016/j.geoderma.2020.114227.

Demattê, J.A.M., Dotto, A.C., Paiva, A.F.S., Sato, M.V., Dalmolin, R.S.D., de Araújo, M.d. S.B., da Silva, E.B., Nanni, M.R., ten Caten, A., Noronha, N.C., Lacerda, M.P.C., de Araújo Filho, J.C., Rizzo, R., Bellinaso, H., Francelino, M.R., Schaefer, C.E.G.R., Vicente, L.E., dos Santos, U.J., de Sá Barretto Sampaio, E.V., Menezes, R.S.C., de Souza, J.J.L.L., Abrahão, W.A.P., Coelho, R.M., Grego, C.R., Lani, J.L., Fernandes, A. R., Gonçalves, D.A.M., Silva, S.H.G., de Menezes, M.D., Curi, N., Couto, E.G., dos Anjos, L.H.C., Ceddia, M.B., Pinheiro, É.F.M., Grunwald, S., Vasques, G.M., Marques Júnior, J., da Silva, A.J., Barreto, M.C.d.V., Nóbrega, G.N., da Silva, M.Z., de Souza, S.F., Valladares, G.S., Viana, J.H.M., da Silva Terra, F., Horák-Terra, I., Fiorio, P.R., da Silva, R.C., Frade Júnior, E.F., Lima, R.H.C., Alba, J.M.F., de Souza Junior, V.S., Brefin, M.D.L.M.S., Ruivo, M.D.L.P., Ferreira, T.O., Brait, M.A., Caetano, N.R., Bringhenti, I., de Sousa Mendes, W., Safanelli, J.L., Guimarães, C.C.B., Poppiel, R.R., e Souza, A.B., Quesada, C.A., do Couto, H.T.Z., 2019. The Brazilian Soil Spectral Library (BSSL): A general view, application and challenges. Geoderma 354, 113793. https://doi.org/10.1016/j.geoderma.2019.05.043.

Demattê, J.A.M., Nanni, M.R., Formaggio, A.R., Epiphanio, J.C.N., 2007. Spectral reflectance for the mineralogical evaluation of Brazilian low clay activity soils. Int. J. Remote Sens. 28 (20), 4537–4559. https://doi.org/10.1080/01431160701250408.

Demattê, J.A.M., Ramirez-Lopez, L., Marques, K.P.P., Rodella, A.A., 2017. Chemometric soil analysis on the determination of specific bands for the detection of magnesium and potassium by spectroscopy. Geoderma 288, 8–22. https://doi.org/10.1016/j.geoderma.2016.11.013.

Diek, S., Schaepman, M., de Jong, R., 2016. Creating Multi-Temporal Composites of Airborne Imaging Spectroscopy Data in Support of Digital Soil Mapping. Remote Sens. 8, 906. https://doi.org/10.3390/rs8110906.

Ding, Z., Kheir, A.M.S., Ali, M.G.M., Ali, O.A.M., Abdelaal, A.I.N., Lin, X., Zhou, Z., Wang, B., Liu, B., He, Z., 2020. The integrated effect of salinity, organic amendments, phosphorus fertilizers, and deficit irrigation on soil properties, phosphorus fractionation and wheat productivity. Sci. Rep. 10, 1–13. https://doi.org/10.1038/s41598-020-59650-8.

Doran, J.W., Parkin, T.B., 1994. Defining and assessing soil quality. Defin. soil Qual. a Sustain. Environ. https://doi.org/10.2136/sssaspecpub35.c1.

Drucker, H., Burges, C.J.C., Kaufman, L., Smola, A.J., Vapnik, V., 1997. Support Vector Regression Machines. In: Mozer, M.C., Jordan, M.I., Petsche, T. (Eds.), Advances in Neural Information Processing Systems 9. MIT Press, pp. 155–161.

Eldridge, D.J., Reed, S., Travers, S.K., Bowker, M.A., Maestre, F.T., Ding, J., Havrilla, C., Rodriguez-Caballero, E., Barger, N., Weber, B., Antoninka, A., Belnap, J., Chaudhary, B., Faist, A., Ferrenberg, S., Huber-Sannwald, E., Malam Issa, O., Zhao, Y., 2020. The pervasive and multifaceted influence of biocrusts on water in the world's drylands. Glob. Chang. Biol. 26 (10), 6003–6014.

FAO, 2019. The State of Food and Agriculture 2019, The State of Food and Agriculture 2019. Food and Agriculture Organization of the United Nations, Rome. http://doi.org/10.4060/ca6030en.

Feingersh, T., Dor, E.B., 2015. SHALOM - A Commercial Hyperspectral Space Mission. In: Optical Payloads for Space Missions. John Wiley & Sons Ltd, Chichester, UK, pp. 247–263. https://doi.org/10.1002/9781118945179.ch11.

Foley, J.A., DeFries, R., Asner, G.P., Barford, C., Bonan, G., Carpenter, S.R., Chapin, F.S., Coe, M.T., Daily, G.C., Gibbs, H.K., Helkowski, J.H., Holloway, T., Howard, E.A., Kucharik, C.J., Monfreda, C., Patz, J.A., Prentice, I.C., Ramankutty, N., Snyder, P.K., 2005. Global Consequences of Land Use. Science (80-.) 309 (5734), 570–574.

Freschet, G.T., Barthès, B.G., Brunet, D., Hien, E., Masse, D., 2011. Use of Near Infrared Reflectance Spectroscopy (NIRS) for Predicting Soil Fertility and Historical Management. Commun. Soil Sci. Plant Anal. 42 (14), 1692–1705. https://doi.org/10.1080/00103624.2011.584597.

Gholizadeh, A., Borůvka, L., Saberioon, M., Vašát, R., 2013. Visible, near-infrared, and mid-infrared spectroscopy applications for soil assessment with emphasis on soil organic matter content and quality: State-of-the-art and key issues. Appl. Spectrosc. 67 (12), 1349–1362.

Goetz, A.F.H., Vane, G., Solomon, J.E., Rock, B.N., 1985. Imaging spectrometry for earth remote sensing. Science (80-.) 228 (4704), 1147–1153.

Groenendyk, D.G., Ferré, T.P.A., Thorp, K.R., Rice, A.K., 2015. Hydrologic-Process-Based Soil Texture Classifications for Improved Visualization of Landscape Function. PLoS One 10, e0131299. http://doi.org/10.1371/journal.pone.0131299.

Guanter, L., Kaufmann, H., Segl, K., Foerster, S., Rogass, C., Chabrillat, S., Kuester, T., Hollstein, A., Rossner, G., Chlebek, C., Straif, C., Fischer, S., Schrader, S., Storch, T., Heiden, U., Mueller, A., Bachmann, M., Mühle, H., Müller, R., Habermeyer, M., Ohndorf, A., Hill, J., Buddenbaum, H., Hostert, P., van der Linden, S., Leitão, P., Rabe, A., Doerffer, R., Krasemann, H., Xi, H., Mauser, W., Hank, T., Locherer, M., Rast, M., Staenz, K., Sang, B., 2015. The EnMAP Spaceborne Imaging Spectroscopy Mission for Earth Observation. Remote Sens. 7, 8830–8857. https://doi.org/10.3390/rs70708830.

Haynes, R.J., Naidu, R., 1998. Influence of lime, fertilizer and manure applications on soil organic matter content and soil physical conditions : a review. 123–137.

Haubrock, S.N., Chabrillat, S., Kuhnert, M., Hostert, P., Kaufmann, H., 2008. Surface soil moisture quantification and validation based on hyperspectral data and field measurements. Journal of Applied Remote Sensing 2. https://doi.org/10.1117/1.3059191.

He, T., Wang, J., Lin, Z., Cheng, Y.e., 2009. Spectral features of soil organic matter. Geo-Spatial Inf. Sci. 12 (1), 33–40. https://doi.org/10.1007/s11806-009-0160-x.

Hengl, T., Nussbaum, M., Wright, M.N, Heuvelink, G.B.M., Gräler, B., 2018. Random forest as a generic framework for predictive modeling of spatial and spatio-temporal variables. PeerJ 6. https://doi.org/10.7717/peerj.5518.

Hotelling, H., 1933. Analysis of a complex of statistical variables into principal components. J. Educ. Psychol. 24 (6), 417–441. https://doi.org/10.1037/h0071325.

Hu, G.-M., Ding, R.-X., Li, Y.-B., Shan, J.-F., Yu, X.-T., Feng, W., 2017. Role of flood discharge in shaping stream geometry: Analysis of a small modern stream in the Uinta Basin. USA. J. Palaeogeogr. 6 (1), 84–95.

Idowu, O.J., van Es, H.M., Abawi, G.S., Wolfe, D.W., Ball, J.I., Gugino, B.K., Moebius, B. N., Schindelbeck, R.R., Bilgili, A.V., 2008. Farmer-oriented assessment of soil quality using field, laboratory, and VNIR spectroscopy methods. Plant Soil 307 (1-2), 243–253. https://doi.org/10.1007/s11104-007-9521-0.

Idowu, O.J., van Es, H.M., Abawi, G.S., Wolfe, D.W., Schindelbeck, R.R., Moebius-Clune, B.N., Gugino, B.K., 2009. Use of an integrative soil health test for evaluation of soil management impacts. Renew. Agric. Food Syst. 24 (3), 214–224. https://doi.org/10.1017/S1742170509990068.

Iglewicz, B., 2011. Summarizing Data with Boxplots, in: International Encyclopedia of Statistical Science. Springer Berlin Heidelberg, pp. 1572–1575. http://doi.org/10.1007/978-3-642-04898-2_582.

Jia, W., Pang, Y., Tortini, R., Schläpfer, D., Li, Z., Roujean, J.L., 2020. A kernel-driven BRDF approach to correct airborne hyperspectral imagery over forested areas with rugged topography. Remote Sens. 12, 432. https://doi.org/10.3390/rs12030432.

Johnston, R.M., Barry, S.J., Bleys, E., Bui, E.N., Moran, K.C.J., Simon, D.A.P., Carlile, P., McKenzie, N.J., Henderson, B.L., Chapman, G., Imhoff, M., Maschmedt, D., Howe, D., Grose, C., Schoknecht, N., Powell, B., Grundy, M., 2003. ASRIS: the database. Soil Res. 41, 1021–1036. https://doi.org/10.1071/SR02033.

Jolliffe, I.T., Cadima, J., Cadima, J., 2016. Principal component analysis : a review and recent developments Subject Areas : Author for correspondence.

Kanning, M., Siegmann, B., Jarmer, T., 2016. Regionalization of uncovered agricultural soils based on organic carbon and soil texture estimations. Remote Sens. 8 (11), 927. https://doi.org/10.3390/rs8110927.

Karlen, D.L., Ditzler, C.A., Andrews, S.S., 2003. Soil quality: why and how? Geoderma 114 (3-4), 145–156.

Karlen, D.L., Mausbach, M.J., Doran, J.W., Cline, R.G., Harris, R.F., Schuman, G.E., 1997. Soil Quality: A Concept, Definition, and Framework for Evaluation (A Guest Editorial). Soil Sci. Soc. Am. J. 61 (1), 4–10. https://doi.org/10.2136/sssaj1997.03615995006100010001x.

Kettler, T.A., Doran, J.W., Gilbert, T.L., 2001. Simplified Method for Soil Particle-Size Determination to Accompany Soil-Quality Analyses. Soil Sci. Soc. Am. J. 65 (3), 849–852. https://doi.org/10.2136/sssaj2001.653849x.

Kinoshita, R., Moebius-Clune, B.N., Es, H.M., Hively, W.D., Bilgilis, A.V., 2012. Strategies for Soil Quality Assessment Using Visible and Near-Infrared Reflectance Spectroscopy in a Western Kenya Chronosequence. Soil Sci. Soc. Am. J. 76 (5), 1776–1788. https://doi.org/10.2136/sssaj2011.0307.

Kothari, C., 2004. Research methodology: methods and techniques, New Age International. http://196.29.172.66:8080/jspui/bitstream/123456789/2574/1/Research%20Methodology.pdf.

Kuhn, M., 2020. caret: Classification and Regression Training.

Lal, R., 2011. Soil health and climate change: an overview. In: Soil Health and Climate Change. Springer, pp. 3–24.

Gozukara, G., Acar, M., Ozlu, E., Dengiz, O., Hartemink, A.E., Zhang, Y., 2022. A soil quality index using Vis-NIR and pXRF spectra of a soil profile. CATENA 211. https://doi.org/10.1016/j.catena.2021.105954.

Greenland, D.J., Gregory, P.J., Nye, P.H., Lal, R., 1997. Degradation and resilience of soils. Philos. Trans. R. Soc. B Biol. Sci. 352 (1356), 997–1010. https://doi.org/10.1098/rstb.1997.0078.

Lee, C.M., Cable, M.L., Hook, S.J., Green, R.O., Ustin, S.L., Mandl, D.J., Middleton, E.M., 2015. An introduction to the NASA Hyperspectral InfraRed Imager (HyspIRI) mission and preparatory activities. Remote Sens. Environ. 167, 6–19. https://doi.org/10.1016/j.rse.2015.06.012.

Levi, N., Hillel, N., Zaady, E., Rotem, G., Ziv, Y., Karnieli, A., Paz-Kagan, T., 2021. Soil quality index for assessing phosphate mining restoration in a hyper-arid environment. Ecol. Indic. 125, 107571. https://doi.org/10.1016/j.ecolind.2021.107571.

Levi, N., Karnieli, A., Paz-Kagan, T., 2020. Using reflectance spectroscopy for detecting land-use effects on soil quality in drylands. Soil Tillage Res. 199, 104571. https://doi.org/10.1016/j.still.2020.104571.

Leys, C., Ley, C., Klein, O., Bernard, P., Licata, L., 2013. Journal of Experimental Social Psychology Detecting outliers: Do not use standard deviation around the mean, use absolute deviation around the median. 4–6.

Li, Z., 2020. Selenium-enriched soil mapping using airborne SASI images. Geoderma 363, 114133. https://doi.org/10.1016/j.geoderma.2019.114133.
Lima, G.C., Silva, M.L.N., Freitas, D.A.F.d., Cândido, B.M., Curi, N., Oliveira, M.S.d., 2016. Spatialization of soil quality index in the Sub-Basin of Posses. Extrema, Minas Gerais. 20 (1), 78–84. https://doi.org/10.1590/1807-1929/agriambi.v20n1p78-84.
Loizzo, R., Guarini, R., Longo, F., Scopa, T., Formaro, R., Facchinetti, C., Varacalli, G., 2018. Prisma: The Italian hyperspectral mission, in: International Geoscience and Remote Sensing Symposium (IGARSS). Institute of Electrical and Electronics Engineers Inc., pp. 175–178. http://doi.org/10.1109/IGARSS.2018.8518512.
Lugassi, R., Goldshleger, N., Chudnovsky, A., 2017. Studying Vegetation Salinity: From the Field View to a Satellite-Based Perspective 1–16. http://doi.org/10.3390/rs9020122.
Marques, K.PP., Rizzo, R., Carnieletto Dotto, A., Souza, A.B.e., Mello, F.AO., Neto, L.GM., Anjos, L.H.C.D., Demattê, J.AM., 2019. How qualitative spectral information can improve soil profile classification? J. Near Infrared Spectrosc. 27 (2), 156–174. https://doi.org/10.1177/0967033518821965.
Masto, R.E., Chhonkar, P.K., Purakayastha, T.J., Patra, A.K., Singh, D., 2008. Soil quality indices for evaluation of long-term land use and soil management practices in semi-arid sub-tropical India. L. Degrad. Dev. 19 (5), 516–529.
Masto, R.E., Chhonkar, P.K., Singh, D., Patra, A.K., 2007. Soil quality response to long-term nutrient and crop management on a semi-arid Inceptisol. Agric. Ecosyst. Environ. 118 (1-4), 130–142. https://doi.org/10.1016/j.agee.2006.05.008.
Matsunaga, T., Iwasaki, A., Tsuchida, S., Tanii, J., Kashimura, O., Nakamura, R., Yamamoto, H., Tachikawa, T., Rokugawa, S., 2013. Current status of Hyperspectral Imager Suite (HISUI). In: International Geoscience and Remote Sensing Symposium (IGARSS), pp. 3510–3513. https://doi.org/10.1109/IGARSS.2013.6723586.
McBartney, A.B., Mendonca Santos, M.L., Minasny, B., 2003. On digital soil mapping. Geoderma. https://doi.org/10.1016/S0016-7061(03)00223-4.
Mcbratney, A.B., Minasny, B., 2016. Why you don't need to use RPD By Budiman Minasny & Alex. McBratney University of Sydney.
Metzger, M.J., Rounsevell, M.D.A., Acosta-Michlik, L., Leemans, R., Schröter, D., 2006. The vulnerability of ecosystem services to land use change. Agric. Ecosyst. Environ. 114 (1), 69–85. https://doi.org/10.1016/j.agee.2005.11.025.
Meyer, D., Dimitriadou, E., Hornik, K., Weingessel, A., Leisch, F., 2019. e1071: Misc Functions of the Department of Statistics, Probability Theory Group (Formerly: E1071), TU Wien.
Michel, S., Gamet, P., Lefevre-Fonollosa, M.J., 2011. HYPXIM A hyperspectral satellite defined for science, security and defence users, in: Workshop on Hyperspectral Image and Signal Processing, Evolution in Remote Sensing. http://doi.org/10.1109/WHISPERS.2011.6080864.
Miles, J., 2005. R-Squared, Adjusted R-Squared. Encycl. Stat. Behav. Sci. http://doi.org/10.1002/0470013192.BSA526.
Moebius-Clune, B.N., 2017. Comprehensive Assessment of Soil Health.
Moebius-Clune, B.N., Moebius-Clune, D., Gugino, B., Idowu, O., Schindelbeck, R., Ristow, A., van Es, H., Thies, J., Shayler, H., McBride, M., Wolfe, D., Abawi, G., 2016. Comprehensive Assessment of Soil Health - The Cornell Framework Manual. http://doi.org/10.1080/00461520.2015.1125787.
Moreira, L.C.J., Teixeira, A.D.S., Galvão, L.S., 2015. Potential of multispectral and hyperspectral data to detect saline-exposed soils in Brazil. GIScience Remote Sens. 52 (4), 416–436. https://doi.org/10.1080/15481603.2015.1040227.
Morón, A., Cozzolino, D., 2007. Measurement of Phosphorus in Soils by Near Infrared Reflectance Spectroscopy: Effect of Reference Method on Calibration. http://doi.org/10.1080/00103620701548498 38, 1965–1974. http://doi.org/10.1080/00103620701548498.
Mourad, M., Bertrand-Krajewski, J.-L., Chebbo, G., 2005. Calibration and validation of multiple regression models for stormwater quality prediction: Data partitioning, effect of dataset size and characteristics. Water Sci. Technol. 52 (3), 45–52. https://doi.org/10.2166/wst.2005.0060.
Norman, R.J., Stucki, J.W., 1981. The Determination of Nitrate and Nitrite in Soil Extracts by Ultraviolet Spectrophotometry 1. Soil Sci. Soc. Am. J. 45 (2), 347–353. https://doi.org/10.2136/sssaj1981.03615995004500020024x.
Nussbaum, M., Spiess, K., Baltensweiler, A., Grob, U., Keller, A., Greiner, L., Schaepman, M.E., Papritz, A., 2018. Evaluation of digital soil mapping approaches with large sets of environmental covariates. SOIL 4, 1–22. https://doi.org/10.5194/soil-4-1-2018.
Ohana-levi, N., Paz-kagan, T., Panov, N., Peeters, A., Tsoar, A., Karnieli, A., Paz-kagan, T., Panov, N., Peeters, A., Tsoar, A., 2018. Time series analysis of vegetation-cover response to environmental factors and residential development in a dryland region. GIScience Remote Sens. 00, 1–26. https://doi.org/10.1080/15481603.2018.1519093.
Olsvig-Whittaker, L., Walczak, M., Jobse, D., Boeken, B., 2012. Patterns in Habitat Type, Species Richness and Community Composition at Avdat Lter. Israel. J. Landsc. Ecol. 5, 5–23. https://doi.org/10.2478/v10285-012-0056-6.
Ong, C., Carrère, V., Chabrillat, S., Clark, R., Hoefen, T., Kokaly, R., Marion, R., Souza Filho, C.R., Swayze, G., Thompson, D.R., 2019. Imaging Spectroscopy for the Detection, Assessment and Monitoring of Natural and Anthropogenic Hazards 40, 431–470. http://doi.org/10.1007/s10712-019-09523-1.
Orgiazzi, A., Ballabio, C., Panagos, P., Jones, A., Fernández-Ugalde, O., 2018. LUCAS Soil, the largest expandable soil dataset for Europe: a review. Eur. J. Soil Sci. 69 (1), 140–153. https://doi.org/10.1111/ejss.12499.
Ou, D., Tan, K., Lai, J., Jia, X., Wang, X., Chen, Y.u., Li, J., 2021. Semi-supervised DNN regression on airborne hyperspectral imagery for improved spatial soil properties prediction. Geoderma 385, 114875. https://doi.org/10.1016/j.geoderma.2020.114875.
Padarian, J., Minasny, B., McBratney, A.B., 2019. Using deep learning to predict soil properties from regional spectral data. Geoderma Reg. 16, e00198. https://doi.org/10.1016/j.geodrs.2018.e00198.
Pansu, M., Gautheyrou, J., 2006. Organic Forms of Nitrogen, Mineralizable Nitrogen (and Carbon). In: Handbook of Soil Analysis. Springer, Berlin Heidelberg, pp. 497–547. https://doi.org/10.1007/978-3-540-31211-6_14.
Paz-Kagan, T., DeMalach, N., Zaady, E., Shachak, M., 2019. Resource redistribution effects on annual plant communities in a runoff harvesting system in dryland. J. Arid Environ. 171, 103984. https://doi.org/10.1016/j.jaridenv.2019.05.012.
Paz-kagan, T., Ohana-levi, N., Herrmann, I., Zaady, E., Henkin, Z., Karnieli, A., 2016. Catena Grazing intensity effects on soil quality : A spatial analysis of a Mediterranean grassland. Catena 146, 100–110. https://doi.org/10.1016/j.catena.2016.04.020.
Paz-Kagan, T., Ohana-Levi, N., Shachak, M., Zaady, E., Karnieli, A., 2017. Ecosystem effects of integrating human-made runoff-harvesting systems into natural dryland watersheds. J. Arid Environ. 147, 133–143. https://doi.org/10.1016/j.jaridenv.2017.07.015.
Paz-Kagan, T., Shachak, M., Zaady, E., Karnieli, A., 2014. A spectral soil quality index (SSQI) for characterizing soil function in areas of changed land use. Geoderma 230–231, 171–184. https://doi.org/10.1016/j.geoderma.2014.04.003.
Paz-Kagan, T., Zaady, E., Salbach, C., Schmidt, A., Lausch, A., Zacharias, S., Notesco, G., Ben-Dor, E., Karnieli, A., 2015. Mapping the spectral soil quality index (SSQI) using airborne imaging spectroscopy. Remote Sens. 7, 15748–15781. https://doi.org/10.3390/rs71115748.
Pelta, R., Carmon, N., Ben-Dor, E., 2019. A machine learning approach to detect crude oil contamination in a real scenario using hyperspectral remote sensing. Int. J. Appl. Earth Obs. Geoinf. 82, 101901. https://doi.org/10.1016/j.jag.2019.101901.
Rahimi, H., Pazira, E., Tajik, F., 2000. Effect of soil organic matter, electrical conductivity and sodium adsorption ratio on tensile strength of aggregates. Soil Tillage Res. 54 (3-4), 145–153. https://doi.org/10.1016/S0167-1987(00)00086-6.
Rinot, O., Levy, G.J., Steinberger, Y., Svoray, T., Eshel, G., 2019. Soil health assessment: A critical review of current methodologies and a proposed new approach. Sci. Total Environ. 648, 1484–1491. https://doi.org/10.1016/J.SCITOTENV.2018.08.259.
Roades, J.D., 1982. Soluble salts, in: Methods of Soil Analysis, Part 2, Chemical and Microbiological Properties, 2nd Ed. ASA-SSSA, Agronomy monograph 9, pp. 137–179.
Robbins, C.W., 1984. Sodium adsorption ratio-exchangeable sodium percentage relationships in a high potassium saline-sodic soil. Irrig. Sci. 5, 173–179. https://doi.org/10.1007/BF00264606.
Chutipong, R., Saowanuch, T., Sumitra, W., 2018. In situ near-infrared spectroscopy for soil organic matter prediction in paddy soil, pasak watershed, thailand. Plant, Soil Environ. 64 (No. 2), 70–75. https://doi.org/10.17221/716/2017-PSE.
Rosero-Vlasova, O.A., Pérez-Cabello, F., Montorio Llovería, R., Vlassova, L., 2016. Assessment of laboratory VIS-NIR-SWIR setups with different spectroscopy accessories for characterisation of soils from wildfire burns. Biosyst. Eng. 152, 51–67. https://doi.org/10.1016/j.biosystemseng.2016.06.011.
Rossel, R.A.V., Behrens, T., 2010. Using data mining to model and interpret soil diffuse reflectance spectra. Geoderma 158 (1-2), 46–54. https://doi.org/10.1016/j.geoderma.2009.12.025.
Saygin, S.D., 2018. Strategies to Enhance Sustainability of Land Resources in Arid Regions, in: Arid Environments and Sustainability. InTech. http://doi.org/10.5772/intechopen.72492.
Schindelbeck, R.R., van Es, H.M., Abawi, G.S., Wolfe, D.W., Whitlow, T.L., Gugino, B.K., Idowu, O.J., Moebius-Clune, B.N., 2008. Comprehensive assessment of soil quality for landscape and urban management. Landsc. Urban Plan. 88 (2-4), 73–80. https://doi.org/10.1016/j.landurbplan.2008.08.006.
Schlapfer, D., Richter, R., Feingersh, T., 2015. Operational BRDF effects correction for wide-field-of-view optical scanners (BREFCOR). IEEE Trans. Geosci. Remote Sensing 53 (4), 1855–1864.
Schmid, T., Koch, M., Gumuzzio, J., Medel, I., 2005. Field and imaging spectroscopy to determine soil degradation stages in semi-arid terrestrial ecosystems.
Schmid, T., Rodríguez-Rastrero, M., Escribano, P., Palacios-Orueta, A., Ben-Dor, E., Plaza, A., Milewski, R., Huesca, M., Bracken, A., Cicuéndez, V., Pelayo, M., Chabrillat, S., Schmid, T., Rodríguez-Rastrero, M., Pelayo, M., 2016. Characterization of Soil Erosion Indicators Using Hyperspectral Data From a Mediterranean Rainfed Cultivated Region. IEEE J. Sel. Top. Appl. EARTH Obs. Remote Sens. 9, 845. https://doi.org/10.1109/JSTARS.2015.2462125.
Scrimgeour, C., 2008. Soil Sampling and Methods of Analysis (Second Edition). Edited by M. R. Carter and E. G. Gregorich. Boca Raton, Fl, USA: CRC Press (2008), pp. 1224, £85.00. ISBN-13: 978-0-8593-3586-0. Exp. Agric. 44, 437–437. http://doi.org/10.1017/s0014479708006546.
Shapiro, M.B., 2006. Soils of Israel. Eurasian Soil Sci. 39 (11), 1170–1175. https://doi.org/10.1134/S1064229306110032.
Shi, P., Castaldi, F., van Wesemael, B., Van Oost, K., 2020. Large-Scale, High-Resolution Mapping of Soil Aggregate Stability in Croplands Using APEX Hyperspectral Imagery. Remote Sens. 12, 666. https://doi.org/10.3390/rs12040666.
Shi, Q.i., Niu, G., Lin, Q., Xu, T., Li, F., Duan, Y., 2015. Quantitative analysis of sedimentary rocks using laser-induced breakdown spectroscopy: Comparison of support vector regression and partial least squares regression chemometric methods. J. Anal. At. Spectrom. 30 (12), 2384–2393.
Shi, Z., Wang, Q.L., Peng, J., Ji, W.J., Liu, H.J., Li, X., Viscarra Rossel, R.A., 2014. Development of a national VNIR soil-spectral library for soil classification and prediction of organic matter concentrations. Sci. China Earth Sci. 57 (7), 1671–1680. https://doi.org/10.1007/s11430-013-4808-x.
Singer, A., 2007. The soils of Israel, The Soils of Israel. Springer Berlin Heidelberg. http://doi.org/10.1007/978-3-540-71734-8.

Singh, K.P., Malik, A., Mohan, D., Sinha, S., Singh, V.K., 2005. Chemometric data analysis of pollutants in wastewater—a case study. Anal. Chim. Acta 532 (1), 15–25.
Singh, S., Kasana, S.S., 2019. Estimation of soil properties from the EU spectral library using long short-term memory networks. Geoderma Reg. 18, e00233. https://doi.org/10.1016/j.geodrs.2019.e00233.
Srivastava, N., Hinton, G., Krizhevsky, A., Sutskever, I., Salakhutdinov, R., 2014. Dropout: A simple way to prevent neural networks from overfitting. J. Mach. Learn. Res. 15, 1929–1958.
Stafford, A.D., Kusumo, B.H., Jeyakumar, P., Hedley, M.J., Anderson, C.W.N., 2018. Cadmium in soils under pasture predicted by soil spectral reflectance on two dairy farms in New Zealand. Geoderma Reg. 13, 26–34. https://doi.org/10.1016/j.geodrs.2018.03.001.
Stevens, A., van Wesemael, B., Vandenschrick, G., Touré, S., Tychon, B., 2006. Detection of Carbon Stock Change in Agricultural Soils Using Spectroscopic Techniques. Soil Sci. Soc. Am. J. 70 (3), 844–850.
Stoner, E.R., Baumgardner, M.F., 1981. Characteristic Variations in Reflectance of Surface Soils. Soil Sci. Soc. Am. J. 45 (6), 1161–1165.
Svoray, T., Hassid, I., Atkinson, P.M., Moebius-Clune, B.N., van Es, H.M., 2015. Mapping Soil Health over Large Agriculturally Important Areas. Soil Sci. Soc. Am. J. 79 (5), 1420–1434.
Taylor, G.R., 2004. Field and image spectrometry for soil mapping. In: 12th Australian Remote Sensing Conference, Fremantle, WA, Australia.
Thissen, U., Pepers, M., Üstün, B., Melssen, W.J., Buydens, L.M.C., 2004. Comparing support vector machines to PLS for spectral regression applications. Chemom. Intell. Lab. Syst. 73 (2), 169–179. https://doi.org/10.1016/j.chemolab.2004.01.002.
Tsakiridis, N.L., Chadoulos, C.G., Theocharis, J.B., Ben-Dor, E., C. Zalidis, G., 2020. A three-level Multiple-Kernel Learning approach for soil spectral analysis. Neurocomputing 389, 27–41. http://doi.org/10.1016/j.neucom.2020.01.008.
Tscharntke, T., Klein, A.M., Kruess, A., Steffan-Dewenter, I., Thies, C., Teja Tscharntke,* Alexandra M. Klein, Andreas Kruess, I.S.-D., C.T., 2005. REVIEWS AND Landscape perspectives on agricultural intensification and biodiversity – ecosystem service management. Ecol. Lett. http://doi.org/10.1111/j.1461-0248.2005.00782.x.
Tucker, C.J., 1979. Red and Photographic Infrared l,lnear Combinations for Monitoring Vegetation, Remote Sens. Environ.
Turner, M.D., 1998. Long-term effects of daily grazing orbits on nutrient availability in Sahelian West Africa: I. Gradients in the chemical composition of rangeland soils and vegetation. J. Biogeogr. 25, 669–682. https://doi.org/10.1046/j.1365-2699.1998.2540669.x.
Tziolas, N., Tsakiridis, N., Ogen, Y., Kalopesa, E., Ben-Dor, E., Theocharis, J., Zalidis, G., 2020. An integrated methodology using open soil spectral libraries and Earth Observation data for soil organic carbon estimations in support of soil-related SDGs. Remote Sens. Environ. 244, 111793. https://doi.org/10.1016/j.rse.2020.111793.
UN-WPP, 2020. World Population Prospects 2019 - Volume II: Demographic Profiles, World Population Prospects 2019 - Volume II: Demographic Profiles. http:doi.org/10.18356/7707d011-en.
Ushey, K., Allaire, J.J., Tang, Y., 2020. reticulate: Interface to "Python.".
Vågen, T.-G., Shepherd, K.D., Walsh, M.G., 2006. Sensing landscape level change in soil fertility following deforestation and conversion in the highlands of Madagascar using Vis-NIR spectroscopy. Geoderma 133 (3-4), 281–294. https://doi.org/10.1016/j.geoderma.2005.07.014.
Vanschoenwinkel, B., Manderick, B., 2005. Appropriate kernel functions for support vector machine learning with sequences of symbolic data. In: Lecture Notes in Computer Science (Including Subseries Lecture Notes in Artificial Intelligence and Lecture Notes in Bioinformatics). Springer, Berlin, Heidelberg, pp. 256–280. https://doi.org/10.1007/11559887_16.
Veum, K.S., Sudduth, K.A., Kremer, R.J., Kitchen, N.R., 2017. Sensor data fusion for soil health assessment. Geoderma 305, 53–61. https://doi.org/10.1016/j.geoderma.2017.05.031.
Veum, K.S., Sudduth, K.A., Kremer, R.J., Kitchen, N.R., 2015. Estimating a Soil Quality Index with VNIR Reflectance Spectroscopy. Soil Sci. Soc. Am. J. 79 (2), 637–649. https://doi.org/10.2136/sssaj2014.09.0390.
Viscarra Rossel, R.A., Behrens, T., Ben-Dor, E., Brown, D.J., Demattê, J.A.M., Shepherd, K.D., Shi, Z., Stenberg, B., Stevens, A., Adamchuk, V., Aïchi, H., Barthès, B.G., Bartholomeus, H.M., Bayer, A.D., Bernoux, M., Böttcher, K., Brodský, L., Du, C.W., Chappell, A., Fouad, Y., Genot, V., Gomez, C., Grunwald, S., Gubler, A., Guerrero, C., Hedley, C.B., Knadel, M., Morrás, H.J.M., Nocita, M., Ramirez-Lopez, L., Roudier, P., Campos, E.M.R., Sanborn, P., Sellitto, V.M., Sudduth, K.A., Rawlins, B.G., Walter, C., Winowiecki, L.A., Hong, S.Y., Ji, W., 2016. A global spectral library to characterize the world's soil. Earth-Science Rev. 155, 198–230. https://doi.org/10.1016/j.earscirev.2016.01.012.
Viscarra Rossel, R.A., Walvoort, D.J.J., McBratney, A.B., Janik, L.J., Skjemstad, J.O., 2006. Visible, near infrared, mid infrared or combined diffuse reflectance spectroscopy for simultaneous assessment of various soil properties. Geoderma 131 (1-2), 59–75. https://doi.org/10.1016/j.geoderma.2005.03.007.
von Lützow, M., Kögel-Knabner, I., Ekschmitt, K., Flessa, H., Guggenberger, G., Matzner, E., Marschner, B., 2007. SOM fractionation methods: Relevance to functional pools and to stabilization mechanisms. Soil Biol. Biochem. 39 (9), 2183–2207. https://doi.org/10.1016/j.soilbio.2007.03.007.
Wacker, A., Landgrebe, D., 1972. Minimum Distance Classification in Remote Sensing. LARS Tech. Reports.
Wang, C.Y., Wang, N., Wang, S., 2000. Regression Analysis When Covariates Are Regression Parameters of a Random Effects Model for Observed Longitudinal Measurements. Biometrics 56, 487–495. https://doi.org/10.1111/j.0006-341X.2000.00487.x.
Wang, J., Peng, J., Li, H., Yin, C., Liu, W., Wang, T., Zhang, H., 2021. Soil salinity mapping using machine learning algorithms with the sentinel-2 MSI in arid areas, China. Remote Sens. 13, 1–14. https://doi.org/10.3390/rs13020305.
Weil, R., Brady, N., 2017. The Nature and Properties of Soils. 15th edition.
Wetschoreck, F., Krabel, T., Krishnamurthy, S., 2020. 8080Labs/Ppscore: Zenodo Release. http://doi.org/10.5281/ZENODO.4091345.
Wienhold, B.J., Karlen, D.L., Andrews, S.S., Stott, D.E., 2009. Protocol for indicator scoring in the soil management assessment framework (SMAF). Renew. Agric. Food Syst. 24 (4), 260–266. https://doi.org/10.1017/S1742170509990093.
Wise, B.M., Gallagher, N.B., Bro, R., Shaver, J.M., Windig, W., Koch, R.S., 2006. PLS_Toolbox Version 4.0 for use with MATLAB ™, Eigenvector Research.
Xuemei, L., Jianshe, L., 2013. Measurement of soil properties using visible and short wave-near infrared spectroscopy and multivariate calibration. Measurement 46 (10), 3808–3814.
Yair, A., Danin, A., 1980. Spatial variations in vegetation as related to the soil moisture regime over an arid limestone hillside, northern Negev. Israel 47 (1), 83–88. https://doi.org/10.1007/BF00541779.
Yang, X.-D., Wang, J., Xu, M.-S., Ali, A., Xu, Y., Lamb, D., Duan, L.-C., Yan, K.-H., Yang, S.-T., 2019. Effects of the ephemeral stream on plant species diversity and distribution in an alluvial fan of arid desert region: An application of a low altitude UAV. PLoS One 14. http://doi.org/10.1371/JOURNAL.PONE.0212057.
Yizhaq, H., Shachak, M., Meron, E., 2020. A model study of terraced riverbeds as novel ecosystems. Sci. Rep. 10 (1) https://doi.org/10.1038/s41598-020-60706-y.
Yuan, Q., Shen, H., Li, T., Li, Z., Li, S., Jiang, Y., Xu, H., Tan, W., Yang, Q., Wang, J., Gao, J., Zhang, L., 2020. Deep learning in environmental remote sensing: Achievements and challenges. Remote Sens. Environ. 241, 111716. https://doi.org/10.1016/j.rse.2020.111716.
Zavarella, L., 2020. Using The Predictive Power Score in R. Medium.
Zhang, C., Mishra, D.R., Pennings, S.C., 2019. Mapping salt marsh soil properties using imaging spectroscopy. ISPRS J. Photogramm. Remote Sens. 148, 221–234. https://doi.org/10.1016/j.isprsjprs.2019.01.006.
Ziv, B., Saaroni, H., Pargament, R., Harpaz, T., Alpert, P., 2014. Trends in rainfall regime over Israel, 1975–2010, and their relationship to large-scale variability. Reg. Environ. Chang. 14 (5), 1751–1764. https://doi.org/10.1007/s10113-013-0414-x.
Žížala, D., Zádorová, T., Kapička, J., 2017. Assessment of Soil Degradation by Erosion Based on Analysis of Soil Properties Using Aerial Hyperspectral Images and Ancillary Data, Czech Republic. Remote Sens. 9, 28. https://doi.org/10.3390/rs9010028.